Faculty of Power and Aeronautical Engineering
Warsaw University of Technology



Institute of Faculty of Power and Aeronautical Engineering

Master's diploma thesis

in the field of study Aerospace Engineering
and specialisation Aerospace Engineering

Validation of Laminar Aeroheating Models for the Mars Science Laboratory Forebody Against T5 Shock-Tunnel Data

Kacper Frelek
student record book number 313668

thesis supervisor
Ph. D. Michał Remer

WARSAW 2026

Validation of Laminar Aeroheating Models for the Mars Science Laboratory Forebody Against T5 Shock-Tunnel Data

Abstract.
This thesis presents a Computational Fluid Dynamics validation study against the shock tunnel aeroheating data for a 70° sphere cone geometry representative of the Mars Science Laboratory forebody. The laminar, zero angle of attack shot 2254 and related conditions are used as benchmarks to assess a family of models that systematically varies spatial order (first vs. second), gas thermal model (single- vs. two-temperature), and wall chemistry (non-catalytic, supercatalytic, Mitcheltree). Thermophysical properties are specified using National Aeronautics and Space Administration nine coefficient polynomials for specific heat and kinetic theory based correlations for viscosity and thermal conductivity, ensuring validity in the high enthalpy tunnel regime. By comparing stagnation point heat fluxes and surface distributions across this model space, the work quantifies the sensitivity of laminar aeroheating predictions to transport, catalysis, and thermal nonequilibrium assumptions. The results identify modelling combinations that best match the T5 measurements and provide practical guidance for Computational Fluid Dynamics based aeroheating analysis of Mars Science Laboratory-class configurations.

Keywords: CFD validation, T5 shock tunnel, 70° sphere-cone, MSL aeroshell, two-temperature model, wall catalysis, aeroheating.

Walidacja laminarnych modeli nagrzewania aerodynamicznego dla przedniej części kadłuba sondy Mars Science Laboratory w oparciu o dane z tunelu uderzeniowego T5

Streszczenie.
W niniejszej pracy przedstawiono walidację obliczeń CFD (ang. Computational Fluid Dynamics) na podstawie danych cieplno przepływowych z tunelu udarowego dla geometrii stożka kulistego o kącie 70°, reprezentującej osłonę czołową sondy MSL (ang. Mars Science Laboratory). Jako przypadek odniesienia wykorzystano eksperyment numer 2254 przy zerowym kącie natarcia oraz pokrewne warunki, na których zweryfikowano rodzinę modeli numerycznych różniących się rzędem dyskretyzacji przestrzennej (pierwszy vs. drugi), modelem termicznym gazu (jednotemperaturowy vs. dwutemperaturowy) oraz opisem chemii przyściennej (ściana niekatalityczna, superkatalityczna, model Mitcheltree). Właściwości termofizyczne zdefiniowano z wykorzystaniem dziewięciowspółczynnikowych wielomianów NASA (ang. National Aeronautics and Space Administration) dla ciepła właściwego oraz zależności opartych na teorii kinetycznej dla lepkości i przewodnictwa cieplnego, co zapewnia poprawność modelu w wysokotemperaturowym zakresie entalpii charakterystycznym dla tunelu T5. Porównanie strumieni ciepła w punkcie stagnacji oraz rozkładów powierzchniowych dla całej rodziny modeli pozwala ilościowo ocenić wrażliwość prognoz laminarnego nagrzewania na założenia dotyczące transportu, katalizy przyściennej i nierównowagi termicznej. Wyniki wskazują kombinacje modeli najlepiej odtwarzające pomiary z T5 i dostarczają praktycznych wskazówek dotyczących wykorzystania obliczeniowej mechaniki płynów w analizach nagrzewania aerodynamicznego dla konfiguracji klasy Marsjańskiego Laboratorium Naukowego.

Słowa kluczowe: walidacja CFD, tunel udarowy T5, stożek kulisty 70°, osłona MSL, model dwutemperaturowy, kataliza przyścienna, aeroheating.

Contents

Nomenclature . . . 7
Symbols . . . 8
Subscripts . . . 11
1. Introduction . . . 12
2. Motivation . . . 13
2.1. Background . . . 13
2.2. Scope of Work . . . 13
2.3. Wall-chemistry models in the T5 study . . . 15
2.3.1. Non-catalytic wall . . . 16
2.3.2. Supercatalytic wall . . . 16
2.3.3. Mitcheltree catalytic model . . . 17
2.3.4. Homogeneous recombination model (not pursued) . . . 17
3. Literature Review . . . 18
3.1. Hypersonic Reentry Physics . . . 18
3.2. High-speed properties . . . 18
3.3. Aerothermodynamics of Hypersonic Vehicles . . . 19
4. Analytical Solution for Heat Flux . . . 20
4.1. Fay-Riddell Correlation . . . 20
4.1.1. Case 2254 . . . 21
4.1.2. Earth Applicability . . . 24
4.1.3. Mars Applicability . . . 24
4.2. Sutton-Graves Correlation . . . 24
4.2.1. Earth Applicability . . . 24
4.2.2. Mars Applicability . . . 24
4.2.3. Case 2254 . . . 24
4.3. Detra-Kemp-Riddell / Detra-Hidalgo-Type Correlation . . . 26
4.3.1. Summary of stagnation point Heating for Shot 2254 . . . 27
5. Geometry Used in the Analysis . . . 29
6. Aerothermodynamics . . . 31
6.1. Energy modes and Heat Transfer . . . 31
6.2. Radiation . . . 32
6.3. Thermal Protection Systems . . . 33
7. Computational Fluid Dynamics . . . 37
7.1. Governing Equation . . . 37
7.2. Turbulence Models . . . 38
7.2.1. RANS . . . 38
7.2.2. SST k-ω Turbulence Model . . . 39

7.2.3. Laminar Model . . . 40
7.3. Boundary Conditions . . . 41
7.3.1. Pressure Far-Field . . . 41
7.3.2. Velocity inlet . . . 42
7.3.3. Pressure outlet . . . 42
7.3.4. Symmetry . . . 43
7.4. Boundary Layer . . . 43
7.5. Fluid Mixture Model . . . 45
8. Mesh Sensitivity . . . 46
8.1. Mesh . . . 49
8.1.1. SST k-ω . . . 49
8.2. Computational Settings . . . 50
9. Solver . . . 51
9.1. Compressibility Models . . . 51
9.2. Energy equation and modes of motion . . . 51
9.3. Species . . . 52
9.4. Freestream Gas Model . . . 53
10.Computational Domain . . . 55
11.Results . . . 56
11.1. Definition of Case Families . . . 56
11.2. Stagnation-Point Heat Flux Comparison . . . 56
11.3. Mesh Adaptation . . . 57
11.4. Temperature Contours . . . 57
11.5. Comparison with Reference Data . . . 67
11.5.1. Non-Catalytic Wall . . . 68
11.5.2. Supercatalytic Wall . . . 68
11.5.3. Mitcheltree Catalytic Wall . . . 68
11.5.4. Obtained Data . . . 69
12.Summary . . . 74
13.Acknowledgements . . . 75
References . . . 76
List of Figures . . . 80
List of Tables . . . 80
List of Appendices . . . 80

Nomenclature

Abbreviations	Description
MSL	Mars Science Laboratory
TPS	Thermal Protection System
CFD	Computational Fluid Dynamics
FR	Fay and Riddell
SG	Sutton Graves
RANS	Reynolds Averaged Navier Stokes
DES	Detached Eddy Simulation
LES	Large Eddy Simulation
DPLR	Data Parallel Line Relaxation (CFD Code)
1T	1 Temperature Model
2T	2 Temperature Model
NASA	National Aeronautics and Space Administration
PICA	Phenolic Impregnated Carbon Ablator
CMC	Ceramic Matrix Composite
LEO	Low Earth Orbit
SST	Shear Stress Transport
BC	Boundary Conditions
AR	Aspect Ratio
AoA	Angle of Attack
SCT	Turbulent Schmidt Number
DNS	Direct Numerical Simulation
LAURA	Langley Aerothermodynamic Upwind Relaxation Algorithm
FS	First-order Scheme
SS	Second-order Scheme

Symbols

Symbol	Description	Units
ρ	Fluid density	$\mathrm{kg/m^3}$
$\vec{v}, \vec{u}$	Velocity vector	m/s
V	Velocity magnitude	m/s
V_n	Normal velocity component	m/s
p	Pressure	Pa
t	Time	s
∇	Gradient operator	—
$\nabla\cdot$	Divergence operator	—
μ	Dynamic viscosity	Pa·s
ν	Kinematic viscosity ($\nu = \mu/\rho$)	$\mathrm{m^2/s}$
$\vec{f}$	Body force per unit mass (e.g., gravity)	$\mathrm{m/s^2}$
$\boldsymbol{\tau}$	Viscous stress tensor	Pa
T	Temperature	K
k	Thermal conductivity / Sutton-Graves constant	W/(m·K) / —
c_p, C_p	Specific heat at constant pressure	J/(kg·K)
c_v	Specific heat at constant volume	J/(kg·K)
e	Internal energy per unit mass	J/kg
e_t	Total energy per unit mass ($e_t = e + \frac{1}{2}\lvert\vec{v}\rvert^2$)	J/kg
$\vec{q}$	Heat flux vector ($\vec{q} = -k\nabla T$)	$\mathrm{W/m^2}$
$q_w, \dot{q}_w$	Wall heat flux	$\mathrm{W/cm^2}$ (or $\mathrm{W/m^2}$)
$q_c, \dot{q}_c$	Convective heat flux	$\mathrm{W/cm^2}$ (or $\mathrm{W/m^2}$)
q_{stag}	Stagnation-point heat flux	$\mathrm{W/cm^2}$
$q_{DH}, \dot{q}_{DH}$	Detra-Hidalgo heat flux	$\mathrm{W/cm^2}$ (or $\mathrm{W/m^2}$)
Φ	Viscous dissipation function	$\mathrm{W/m^3}$
δ_{ij}	Kronecker delta	—
x_i	Spatial coordinate in direction i	m
v_i	Velocity component in direction i	m/s
$\partial/\partial t$	Temporal derivative	$\mathrm{s^{-1}}$
$\vec{v}\cdot\nabla$	Convective derivative operator	$\mathrm{s^{-1}}$
∇^2	Laplacian operator (diffusion)	$\mathrm{m^{-2}}$
$\overline{u}$	Time-independent mean flow term (RANS)	m/s
u'	Time-varying term (RANS)	m/s
Pr	Prandtl number	—
Le	Lewis number	—
R_n	Nose radius	m
R_b	Base radius	m

Symbol	Description	Units
D_b	Base diameter	m
M	Mach number	—
M_n	Normal Mach number	—
β	Local shock angle / Turbulence model constant	deg / —
h	Enthalpy	J/kg
h_0	Stagnation enthalpy	J/kg
h_D	Diffusion/Dissociation enthalpy	J/kg
c_i	Mass fraction of species i	—
X_i	Mole fraction of species i	—
Δh_f°	Standard enthalpy of formation	J/kg
Kn	Knudsen number	—
λ	Molecular mean free path	m
Re	Reynolds number	—
γ	Ratio of specific heats	—
α	Thermal diffusivity / Turbulence model constant	m^2/s / —
D, D_{im}	Mass diffusion coefficients	m^2/s
a	Speed of sound	m/s
R_{spec}	Specific gas constant	J/(kg·K)
R_{univ}	Universal gas constant	J/(mol·K)
M_{CO_2}	Molecular weight of CO_2	kg/mol
L	Characteristic length	m
n	Outward normal vector	—
K_{DH}	Detra-Hidalgo constant	—
μ_t	Turbulent eddy viscosity	Pa·s
$\tilde{\phi}$	Favre-averaged variable	[Variable]
ϕ''	Favre-fluctuation	[Variable]
λ_t	Turbulent thermal conductivity	W/(m·K)
k_{turb}	Turbulent kinetic energy	J/kg
ω	Specific dissipation rate	s^{-1}
P_k	Production of turbulent kinetic energy	kg/(m·s^3)
F_1	Blending function (SST model)	—
σ_k, σ_ω	Turbulence model constants	—
w^-, w^+	Riemann invariants	m/s
s	Specific entropy	J/(kg·K)
$\dot{m}$	Mass flow rate	kg/s
A	Area	m^2
y^+	Dimensionless wall distance	—
u_τ	Friction velocity	m/s

Symbol	Description	Units
y^*	Semi-local wall coordinate	—
Re_{cell}	Cell Reynolds number	—
c_d	Drag coefficient	—

Subscripts

e	Boundary-layer edge conditions
w	Wall conditions
$\infty, 1$	Freestream / Upstream conditions
2	Post-shock conditions
s	Stagnation point conditions
t	Turbulent quantities
0	Total / Stagnation conditions
n	Normal component
$stag$	Stagnation point
E, M	Earth, Mars (e.g., in Sutton-Graves constants)
c	Convective

1. Introduction

In modern planetary entry missions, accurate prediction of hypersonic aerothermodynamic loads is a key driver for the design of robust and mass efficient thermal protection systems. For Mars Science Laboratory (MSL), the unprecedented combination of vehicle size, entry mass and non zero angle of attack leads to severe convective heating environments in a high-enthalpy, reacting CO_2 atmosphere, with boundary-layer transition and possible turbulent augmentation expected before peak heating. Ground-based facilities such as the Caltech T5 reflected shock tunnel were therefore used to generate aeroheating data on sub-scale models of the MSL aeroshell, providing a critical validation dataset for CFD tools and physical models.

This thesis focuses on hypersonic aerothermodynamic analysis of an MSL-like Mars entry configuration (1.1), using a 70° sphere-cone geometry and T5 shock-tunnel conditions as the reference environment. The primary objective is to investigate laminar heat-flux distributions on the windward forebody and to quantify how sensitive the predicted aeroheating is to key modeling choices, including spatial discretisation order, gas thermal model (single- vs. two-temperature) and wall chemistry (non-catalytic, supercatalytic and Mitcheltree catalytic boundary conditions).

By systematically varying these CFD settings and comparing the resulting heat-flux levels and distributions against the T5 measurements reported by Wright [1] the work aims to identify modeling combinations that provide the most reliable laminar aeroheating predictions for MSL-class Mars entries. The resultscan be used to further support future, more advanced studies that include transition and turbulence, and to contribute to reducing modeling uncertainty in TPS design for high-enthalpy CO_2 entry environments.



Figure 1.1. MSL tested geometry [1]

2. Motivation

2.1. Background

Although the role of geometry in reentry aerothermodynamics is important, an equally critical challenge lies in predicting heat flux. Thermal loads during atmospheric entry largely dictate vehicle survivability and performance, driving decisions on material selection, TPS design, and overall mission feasibility. Yet, despite extensive research on reentry flows, relatively few studies specifically isolate and quantify the impact of chosen simulational settings on both local and global heat flux distributions. This gap is important, since without proper choice of previously mentioned parameters, the success of a mission might be questioned.

Accurate heat-flux prediction remains one of the most demanding tasks in CFD. Shock-boundary layer interactions, high-enthalpy effects, and turbulence-radiation coupling generate nonlinear flow behavior, where small modeling choices can lead to large deviations in heating estimates. The choice of turbulence models, wall treatments, and grid resolution plays a decisive role, particularly in predicting stagnation-point heating and localized hot spots. As Wright [1] uses turbulent and laminar models in the article, the shot 2254 that will be main reference shot in this thesis assumes laminar flow. For this reason, the present study not only examines aerodynamic sensitivity to simulational parameters but also places strong emphasis on theoretical analytical solutions.

In the specific context of MSL, this challenge is particularly evident. The combination of high-enthalpy CO_2 flow and high speed flow at zero angle of attack leads to strong bow shocks and increase of heat-flux levels on the forebody and shoulder regions, as documented in the T5 shock-tunnel campaign. These experiments provide a well characterised reference case against which different CFD modeling strategies can be systematically assessed, making them an ideal framework for the present study.

2.2. Scope of Work

The present study builds directly on the shock-tunnel experiments and CFD analysis of Wright, who modeled aeroheating on a 70° sphere-cone representative of the MSL aeroshell using data from the T5 facility at Caltech.[1] In that work, a 5%-scale stainless-steel model was tested in pure CO_2 wind tunnel over a range of reservoir enthalpies and stagnation pressures chosen to span laminar, transitional, and fully turbulent heating regimes along the windward and leeside surfaces.[1]. Freestream conditions for each shot were obtained by nozzle-flow calculations, and the resulting heat-flux distributions were used to validate flight-design CFD tools and to quantify the role of wall catalysis and turbulence modeling in MSL aerothermodynamics.[1]

On the numerical side, Wright employed the DPLR and LAURA Navier-Stokes solvers with finite-rate $CO_2/CO/O_2/C/O$ chemistry, a two-temperature (Park) thermal nonequi-

librium model, and both laminar and RANS turbulence closures (Baldwin-Lomax and Menter SST).[1]. Three wall-chemistry limits were investigated: a non-catalytic wall, a fully catalytic but diffusion-limited Mitcheltree model, and a supercatalytic wall that forces complete recombination to CO_2 at the surface.[1] A key reference case in that study is shot 2254, a high-enthalpy, low-pressure, zero-angle-of-attack configuration for which the flow is nominally laminar over the entire windward side. Figure 2.1 reproduces the laminar centerline heat-transfer distributions reported by Wright for shot 2254 for the three catalysis models, and provides the primary experimental benchmark for the present work.[1]

The present study narrows this broad experimental and numerical context to a more tightly controlled CFD investigation aimed at isolating the impact of selected modeling choices on laminar aeroheating prediction for the specific T5 shot 2254 condition. We consider the same 70° sphere-cone geometry at the freestream enthalpy and pressure corresponding to shot 2254, but restrict attention to a non-ablating, smooth wall and steady laminar flow. Within this framework, we systematically vary three classes of CFD settings: (i) spatial discretization order (first- versus second-order schemes), (ii) gas thermal model (single-temperature versus two-temperature formulations), and (iii) wall-chemistry boundary condition (non-catalytic, Mitcheltree, and supercatalytic), while keeping all other numerical parameters as close as possible to those used by Wright.[1]

The primary objective is not to re-survey the full T5 test matrix, but rather to directly compare the aeroheating data generated by Ansys Fluent with the experimental test data and the CFD results from DPLR and LAURA reported in the reference article [1]. Furthermore, the study aims to quantify, for this single well-characterised laminar shot, how much the predicted local and global heating levels change as a function of the different CFD configurations. Particular emphasis is placed on the stagnation region and the integrated windward side heating, where design margins for ablative thermal protection systems are typically tight. Effects such as surface roughness, material ablation, and fully turbulent or transitional boundary layers are therefore excluded, so that the influence of Fluent settings on laminar heat-flux predictions can be assessed in isolation. This allows the results to be translated into a more transparent modeling-uncertainty envelope for future TPS design studies and benchmarked directly against the established experimental data.

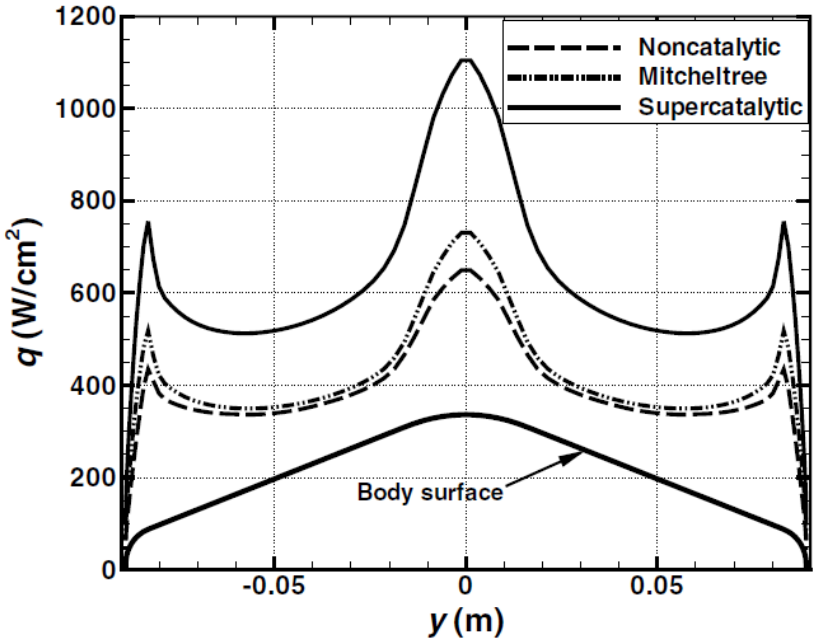


Fig. 5 Predicted catalytic effect on laminar centerline heating for shot 2254.

Figure 2.1. Laminar centerline heat-transfer distributions for T5 shot 2254 from Wright [1], comparing non-catalytic, Mitcheltree, and supercatalytic wall models. This profile serves as the primary experimental reference for the present CFD study.

2.3. Wall-chemistry models in the T5 study

In addition to varying freestream conditions and turbulence modeling, Wright placed particular emphasis on the influence of surface catalysis on the predicted heating levels.[1] For the CO_2 test gas relevant to MSL, three limiting wall-chemistry models were considered: a non-catalytic wall, a fully catalytic but diffusion-limited Mitcheltree model, and a supercatalytic wall. Their effect on the near-wall species composition along the stagnation streamline for shot 2254 is illustrated in Fig. 2.2, which shows the mole fractions of CO_2, CO, O_2, and O as a function of distance from the stagnation point.[1]

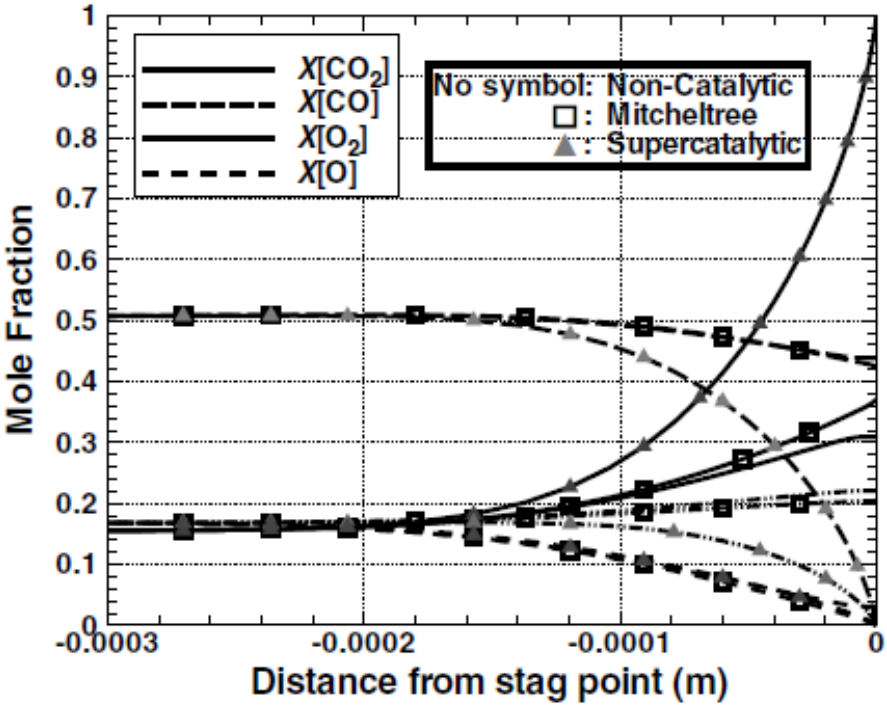


Figure 2.2. Computed mole fractions of CO_2, CO, O_2, and O along the stagnation streamline for shot 2254, comparing non-catalytic, Mitcheltree, and supercatalytic wall models (adapted from Wright[1]).

2.3.1. Non-catalytic wall

In the non-catalytic limit, the surface is assumed to be completely inert with respect to gas-phase species.[1] There is no net production or destruction of CO_2, CO, O_2, nor O at the wall, so the species mass fluxes normal to the surface vanish (apart from what is required to satisfy overall mass conservation). As a result, the composition throughout most of the boundary layer remains close to the post-shock state, and any recombination of dissociated species occurs only through homogeneous gas-phase reactions in the shock layer and boundary layer. In Fig. 2.2, the non-catalytic curves (no symbols) show relatively weak changes in CO_2, CO, and O_2 mole fractions as the wall is approached, and the near-wall CO_2 fraction stays well below unity.[1]

2.3.2. Supercatalytic wall

The supercatalytic model represents the opposite, highly idealised limit, in which the surface is assumed to promote recombination of all incident species so efficiently that the gas at the wall is driven to its lowest-enthalpy state.[1] For the present CO_2 mixture, this is effectively pure CO_2, so the wall boundary condition is imposed by fixing the composition at the surface to $X_{CO_2} = 1$, $X_{CO} = X_{O_2} = X_O = 0$. This is not a finite-rate kinetic model, but rather a Dirichlet condition on species mass fractions that recovers nearly all of the chemical enthalpy stored in dissociated species as sensible heat at the

surface, thereby maximising the catalytic contribution to wall heating. In Fig. 2.2, the supercatalytic solution (solid symbols) exhibits a very steep rise in CO_2 mole fraction and a corresponding decay of CO, O_2, and O as the wall is approached, with X_{CO_2} tending to unity at the surface.[1]

2.3.3. Mitcheltree catalytic model

The Mitcheltree model provides a more physically motivated, finite-rate description of CO_2 recombination at the wall, originally developed in the context of Mars Pathfinder.[1] In this model, recombination proceeds via two surface-reaction pathways involving adsorbed oxygen atoms and carbon monoxide:

$$\mathrm{O} + s \rightarrow \mathrm{O}s, \qquad \mathrm{CO} + s \rightarrow \mathrm{CO}s,$$

$$\mathrm{CO}s + \mathrm{O}s \rightarrow \mathrm{CO_2} + 2s,$$

where s denotes an empty surface site. The wall is assumed to be fully catalytic in the sense that, given sufficient time, all incident CO and O can recombine to CO_2, but the overall rate is limited by diffusion of reactants (CO and O) from the boundary-layer edge to the surface. Under the T5 shot 2254 conditions, much of the oxygen is tied up in O_2 and CO, and the post-shock gas is not fully dissociated, so the diffusive supply of atomic oxygen to the wall is relatively small.[1] Consequently, the Mitcheltree model produces only modest additional CO_2 formation at the wall compared with the non-catalytic case, and the corresponding heating levels remain much closer to the non-catalytic solution than to the supercatalytic upper bound for this particular shot.[1]

2.3.4. Homogeneous recombination model (not pursued)

Wright briefly considered an alternative wall model in which only homogeneous recombination of O atoms to O_2 is allowed in the near-wall region, without direct CO_2 formation at the surface.[1] This mechanism would release less energy per O atom than the CO + O surface reaction embodied in the Mitcheltree model, and therefore lead to even lower heating than the Mitcheltree case. For the purposes of bounding MSL aeroheating, this model was deemed less relevant and was not used in the main comparison.[1]

Together, these three wall-chemistry limits (non-catalytic, Mitcheltree, supercatalytic) define a practical envelope for catalytic behaviour in CO_2 shock-tunnel flows: the non-catalytic case provides a conservative lower bound on heating, the supercatalytic model a conservative upper bound, and the Mitcheltree model offers a diffusion-limited finite-rate intermediate that can, depending on freestream enthalpy and degree of dissociation, lie closer to either bound.[1]

3. Literature Review

3.1. Hypersonic Reentry Physics

The transition to hypersonic flow is a crucial challenge in aerothermal engineering, where conventional aerodynamic assumptions break down and new physical phenomena emerge. As the most common approach suggested to define it as M>5 flow, the hypersonic regime can be characterised by more accurate physical phenomena, which emerge when kinetic energy transforms into thermal energy at sufficiently high magnitudes (Eq. 1) [2].

$$M_n = M \sin\beta \tag{1}$$

Where M is the free-stream Mach number and β the local shock angle, such that the stagnation enthalpy (Eq. 2) drives post-shock translational temperatures high enough to excite molecular vibration and chemistry to the same order as the convective time scale L/V_n [3].

$$h_0 = h + \tfrac{1}{2}V^2 \tag{2}$$

When Eq. 3 is satisfied [3], the flow enters the hypersonic aerothermal regime, immediately behind the shock, vibrational-translational collisions and vibrational-vibrational energy transfer establish a quasi-vibrational temperature only after a finite relaxation period [3].

$$\frac{V_n^2}{2\,C_p\,T_\infty} \gtrsim 5 \tag{3}$$

Dissociation of diatomic species begins when stagnation point temperatures exceeds about $\sim$ 2000 K, and full ionisation occurs above $\sim$8000K. The shock stand-off distance shrinks as M_n rises, intensifying shock-boundary layer coupling and heat flux spikes scaling approximately with $q \propto V_n^3$ [4]. Specific heat $C_p(T)$ varies strongly once internal modes are excited, invalidating perfect-gas assumptions and requiring two- or multi-temperature models. Thus, from an aerothermal standpoint, hypersonic regime truly begins when the normal kinetic energy density $\frac{1}{2}\rho V_n^2$ exceeds the threshold for significant non-ideal effects (Eq. 4):

$$\frac{\frac{1}{2}V_n^2}{R\,T_\infty} \gtrsim \text{5-10.} \tag{4}$$

3.2. High-speed properties

One can distinguish some characteristic physics behaviour that are present during hypersonic reentry. Key aspects of such a flow include dissociation, where molecular atoms break down into atomic species due to high temperatures, influencing thermodynamic

properties. At even higher temperatures, ionisation occurs: gas molecules lose electrons, forming a plasma sheath that can cause communication blackouts for spacecraft. Furthermore, vibrational excitation occurs even before dissociation, as molecules enter higher vibrational energy states, heavily impacting heat transfer and chemical kinetics.

Another factor worth mentioning in high-speed flows is the importance of specific properties and non-dimensional numbers in aerothermodynamics. The Knudsen Number (Kn) is defined as the ratio of the molecular mean free path (λ) to a characteristic length (L), expressed as $Kn = \frac{\lambda}{L}$. It determines whether the flow is in the continuum ($Kn < 0.01$), slip ($0.01 < Kn < 0.1$), transitional ($0.1 < Kn < 10$), or free-molecular regime ($Kn > 10$) [5]. The Reynolds Number (Re) is given by $Re = \frac{\rho UL}{\mu(T)}$, where ρ is density, U is velocity, L is the characteristic length, and $\mu(T)$ is dynamic viscosity. It influences the transition from laminar to turbulent boundary layers, directly affecting heat transfer. The stagnation enthalpy (h_0) represents the total energy per unit mass, which dictates the maximum temperature a surface can reach under given flow conditions. Finally, the specific heat ratio (γ) is defined as the ratio of specific heats (c_p/c_v). This ratio decreases in high-temperature gas flows due to dissociation and excitation effects, and its behavior is dependent on whether the gas is monatomic or diatomic.

The proper selection of these parameters is essential in CFD modeling and experimental validation of hypersonic flows. Besides numerical values, it is important to put special focus on the behaviour of such a flow. One of the phenomena that needs to be observed is also shock wave and boundary layer interactions. For blunt bodies used in reentry vehicles, bow shocks form in front of the vehicle, compressing and heating gas. Depending on the structure of such shock, heating profiles may differ, as strong shock waves lead to intense stagnation heating at the vehicle's nose and shock-boundary layer interactions can cause localized heating peaks and influence transition from laminar to turbulent flow. Another important phenomenon is that the transition from laminar to turbulent flow significantly affects heat transfer rates and structural integrity [6].

3.3. Aerothermodynamics of Hypersonic Vehicles

There are several important factors that need to be observed in a high speed flow, such as aerodynamic heating and thermal loads caused by it. Thermal effects can be divided into convection, radiation, and conduction. Convection in hypersonic flow is expected to be the dominant heating mode, especially when analysing the stagnation point. Although radiation may not be as significant as convection in the lower hypersonic regime, it becomes much more meaningful in highly hypersonic flows when the Mach number is sufficiently high to provide radiative heating from a shock layer. Differing from previously mentioned modes, conduction is not that significant in external aerothermodynamics, as it is the most important for analysing inner structure behaviour and TPS.

Taking into account all parameters is important from TPS modeling point of view,

whether take into account ablative or radiative one. Blunt-body designs reduce peak heating but increase overall drag, while slender shapes reduce drag but suffer from higher localised heating, which leads to another concern, considering the shape effect on heating.

4. Analytical Solution for Heat Flux

Accurate prediction of heat flux is a crucial aspect of reentry aerothermodynamics, and analytical or semi-empirical models remain valuable for validating CFD results. Several classical correlations exist to approximate convective and radiative heating at the stagnation point of blunt bodies. These provide useful benchmarks against which CFD-predicted heating rates can be compared.

4.1. Fay-Riddell Correlation

The Fay-Riddell relation provides a physics-based expression for laminar stagnation point heat transfer in chemically reacting, high-enthalpy fluid. It is derived from boundary-layer theory, so in principle it applies to any gas mixture if one supplies the right transport properties and chemistry model. It accounts for boundary-layer transport properties and species diffusion.

The heat-flux to the wall for a spherical nose can be expressed in three cases [4]: The first equation corresponds to an equilibrium boundary layer [Eq. 5]: In this case, all chemical reactions (dissociation, recombination, ionization) proceed to maintain local thermodynamic equilibrium throughout the boundary layer. Species concentrations and energy modes adjust continuously in response to the local temperature and pressure, so the enthalpy defect term [Eq. 6] enters with an exponent of 0.52, reflecting the rate at which chemical heat release alters the heat flux.

$$q_w = 0.76\,\mathrm{Pr}^{-0.6}\,(\rho_e\mu_e)^{0.4}\,(\rho_w\mu_w)^{0.1}\sqrt{\left(\frac{du_e}{dx}\right)_s}\,(h_{0e}-h_w)\left[1+\left(\mathrm{Le}^{0.52}-1\right)\frac{h_D}{h_{0e}}\right] \tag{5}$$

where

$$h_D = \sum_i c_{i,e}\,(\Delta h_f)_i^\circ \tag{6}$$

The second case corresponds to the frozen boundary layer with catalytic wall [Eq. 7. Here, chemical reactions in the boundary layer are frozen—species concentrations remain fixed at their post-shock values as the gas flows toward the wall.

However, the wall surface is perfectly catalytic, so any radicals reaching it recombine instantly to equilibrium. This surface recombination releases heat back into the gas, hence the Lewis-number exponent of 0.63 modifies the enthalpy defect contribution.

$$q_w = 0.76\,\mathrm{Pr}^{-0.6}\,(\rho_e\mu_e)^{0.4}\,(\rho_w\mu_w)^{0.1}\sqrt{\left(\frac{du_e}{dx}\right)_s}\,(h_{0e}-h_w)\left[1+\left(\mathrm{Le}^{0.63}-1\right)\frac{h_D}{h_{0e}}\right] \tag{7}$$

Last of the listed cases is the frozen boundary layer with noncatalatic wall [Eq. 8], where the gas composition is again frozen in the boundary layer, and the wall is noncatalytic, which means that no surface recombination occurs. Consequently, radicals do not recombine at the surface, removing the enthalpy defect term from the convective difference $(h_{0e} - h_w)$ and replacing it with the simple factor $(1 - h_D/h_{0e})$. This yields the lowest catalytic contribution to the heat flux among the three cases.

$$q_w = 0.76\,\mathrm{Pr}^{-0.6}\,(\rho_e\mu_e)^{0.4}\,(\rho_w\mu_w)^{0.1}\sqrt{\left(\frac{du_e}{dx}\right)_s}\left(1-\frac{h_D}{h_{0e}}\right) \tag{8}$$

where h_0 is total enthalpy, and h_D the diffusion enthalpy. Subscripts e and w denote boundary-layer edge and wall conditions, respectively. The stagnation-line velocity gradient is typically approximated as [Eq. 9][4]:

$$\left(\frac{du_e}{dx}\right)_s \approx \frac{1}{R_n}\sqrt{\frac{2\,(p_e-p_\infty)}{\rho_e}}, \tag{9}$$

Lewis number is calculated from the equation [Eq. 10]:

$$Le = \frac{\alpha}{D} = \frac{\lambda}{\rho D_{im} c_p} \tag{10}$$

Where α is thermal diffusivity, λ is thermal conducitivity D mass diffusivity, D_{im} is the mixture-averaged diffusion coefficient, and c_p here is the specific heat capacity at constant pressure. For gases one can assume for simplicity $Le = 1$

4.1.1. Case 2254

For the shot 2254, an approximate laminar stagnation point heat flux can be obtained using the Fay-Riddell framework together with a simple normal-shock model and Sutherland's law for the viscosity of CO_2. The freestream conditions are taken from Wright [1] and the environment for simplicity of assumptions is taken as CO_2.

$$V_\infty = 3367\,\mathrm{m/s}, \qquad \rho_\infty = 0.03116\,\mathrm{kg/m^3}, \qquad T_\infty \approx 1828\,\mathrm{K}, \qquad h_0 \approx 10.6\times10^6\,\mathrm{J/kg},$$

For the calculations, the effective stagnation radius is taken as a radius of the nose cone of the analyzed geometry, where it is denoted as:

$$R_n = 0.04445\,\mathrm{m}.$$

For the simplification of Fay-Riddell calculations, one can approximate that CO_2 is treated as an ideal gas with

$$R_{CO_2} \approx 188.9\,\mathrm{J/(kg\,K)}, \qquad \gamma \approx 1.30.$$

The static freestream pressure is calculated from the ideal-gas corelation

$$p_\infty = \rho_\infty R_{CO_2} T_\infty \approx 1.08 \times 10^4\,\mathrm{Pa},$$

and the corresponding sound speed and Mach number are

$$a_\infty = \sqrt{\gamma R_{CO_2} T_\infty} \approx 670\,\mathrm{m/s}, \qquad M_\infty = \frac{V_\infty}{a_\infty} \approx 5.0.$$

Along the stagnation streamline, the post-shock edge state is approximated using normal-shock relations for a perfect gas. For an upstream Mach number $M_1 = M_\infty$ one obtains the following:

$$\frac{p_2}{p_1} = 1 + \frac{2\gamma}{\gamma+1}\left(M_1^2 - 1\right), \qquad \frac{\rho_2}{\rho_1} = \frac{(\gamma+1)M_1^2}{2+(\gamma-1)M_1^2}, \qquad \frac{T_2}{T_1} = \frac{p_2/p_1}{\rho_2/\rho_1}.$$

With $M_1 \approx 5.0$ and $\gamma = 1.30$ we have the following:

$$\frac{p_2}{p_1} \approx 28.4, \qquad \frac{\rho_2}{\rho_1} \approx 6.06, \qquad \frac{T_2}{T_1} \approx 4.69,$$

so that the boundary-layer edge state is approximated by

$$p_e \approx p_2 \approx 3.06 \times 10^5\,\mathrm{Pa}, \qquad \rho_e \approx 0.189\,\mathrm{kg/m^3}, \qquad T_e \approx 8.56 \times 10^3\,\mathrm{K}.$$

A cold wall consistent with the article [[1]] analysis is assumed, with

$$T_w = 300\,\mathrm{K}.$$

Approximately the static pressure of the wall as $p_w \approx p_e$, the wall density becomes

$$\rho_w = \frac{p_e}{R_{CO_2} T_w} \approx 5.4\,\mathrm{kg/m^3}.$$

The stagnation-line velocity gradient term from the Fay-Riddell equation is approximated by the Newtonian/Fay-Riddell expression

$$\left(\frac{du_e}{dx}\right)_s = \frac{1}{R_n}\sqrt{\frac{2\left(p_e - p_\infty\right)}{\rho_e}},$$

which, with the values above and $R_n = 0.04445\,\mathrm{m}$, gives

$$\left(\frac{du_e}{dx}\right)_s \approx 4.0 \times 10^4\,\mathrm{s}^{-1}.$$

The classical Fay-Riddell laminar stagnation point heat-flux relation can be written as

$$\dot{q}_w = 0.763\,\mathrm{Pr}^{-0.6}(\rho_e\mu_e)^{0.4}(\rho_w\mu_w)^{0.1}\sqrt{\left(\frac{du_e}{dx}\right)_s}\,(h_{0,e} - h_w)\left[1 + (\mathrm{Le}^{0.52} - 1)\left(\frac{h_D}{h_{0,e}}\right)\right],$$

where Pr is the Prandtl number, Le is the Lewis number, $h_{0,e}$ is the stagnation enthalpy at the edge, h_w is the wall enthalpy and h_D is an effective dissociation enthalpy. For an approximate convective contribution in this CO_2 case, the chemistry bracket is neglected by taking $\mathrm{Le} \approx 1$, so

$$\dot{q}_w \approx 0.763\,\mathrm{Pr}^{-0.6}(\rho_e\mu_e)^{0.4}(\rho_w\mu_w)^{0.1}\sqrt{\left(\frac{du_e}{dx}\right)_s}\,(h_0 - h_w),$$

where the total enthalpy h_0 is taken directly from the test condition (kinetic enthalpy as defined in the T5 analysis) and the wall enthalpy is modeled using a constant-c_p approximation

$$c_p \approx \frac{\gamma}{\gamma - 1}R_{\mathrm{CO_2}}, \qquad h_w = c_p T_w.$$

With $c_p \approx 818\,\mathrm{J/(kg\,K)}$ and $T_w = 300\,\mathrm{K}$ one finds

$$h_w \approx 2.45 \times 10^5\,\mathrm{J/kg}, \qquad \Delta h = h_0 - h_w \approx 1.04 \times 10^7\,\mathrm{J/kg}.$$

Inserting the numerical values for ρ_e, ρ_w, μ_e, μ_w, $\mathrm{Pr} \approx 0.7$, $(du_e/dx)_s$ and Δh into the convective Fay-Riddell expression yields a stagnation point heat flux of order

$$\dot{q}_w \approx 1.1 \times 10^7\,\mathrm{W/m^2} \quad \Rightarrow \quad \dot{q}_w \approx 1.1 \times 10^3\,\mathrm{W/cm^2}.$$

Thus, even with the simplified perfect-gas normal shock, ideal-gas CO_2 thermodynamics, and Sutherland viscosity (extrapolated in temperature and not strictly valid at the lowest and highest temperatures in this flow), the Fay-Riddell convective estimate for shot 2254 lies very close to the laminar super-catalytic DPLR stagnation heat flux of approximately $1100\,\mathrm{W/cm^2}$ cited in the original analysis [1], providing a useful cross-check on both the CFD and the simpler Sutton-Graves/Tauber/Detra correlations.

4.1.2. Earth Applicability

The Fay-Riddell correlation is well-validated for Earth atmospheric entry conditions. Anderson [4] confirms that the FR correlation is based on fundamental boundary-layer theory and has been extensively validated against Earth entry data for air (N_2/O_2) mixtures. The correlation provides accurate stagnation point heating predictions for Earth entry vehicles when proper air thermochemical properties are assumed.

4.1.3. Mars Applicability

The FR correlation is applicable to Mars CO_2 atmospheres, but requires significant modifications. The correlation's physics-based foundation allows it to work for CO_2 atmospheres if accurate high-temperature thermochemical properties, dissociation models, and transport coefficients are provided [7]. However, real-gas effects and CO_2 dissociation chemistry at Mars entry conditions create substantial deviations from standard implementations. Kim et al. [8] emphasise the importance of multi-temperature models for accurate heat transfer predictions in hypersonic flows, supporting the need for updated thermochemical data when applying FR to Mars conditions.

4.2. Sutton-Graves Correlation

For engineering applications, the Sutton-Graves correlation is widely used due to its simplicity. It expresses stagnation convective heat flux as [11]:

$$\dot{q}_c = k\sqrt{\frac{\rho}{R_n}}\,V^3, \tag{11}$$

The result is typically given in $\frac{W}{cm^2}$ for conveniance.

4.2.1. Earth Applicability

The [Eq. 11] can be adjusted to proper environments by choosing the appropriate 'k' parameter. As denoted in the [9], which assumes fully catalytic wall, for the Earth atmoshpere $k = 1.7415 \times 10^{-4}$. For a noncatalytic wall Sutton-Graves equation can be modified and extra assumptions needs to be applied according to known approaches [10].

4.2.2. Mars Applicability

SG correlation is 'k' coefficient dependent. For the Mars conditions one can use constant $k = 1.9027 \times 10^{-4}$ to apply to Eq. (11). As analytical solutions are still being developed and try to minimize the error of it, new approach presented by West and Brandis is also applicable Eq. [11].

4.2.3. Case 2254

For the T5 CO_2 shot 2254, the freestream test-section conditions are

$$V_\infty = 3367\,\mathrm{m/s}, \qquad \rho_\infty = 0.03116\,\mathrm{kg/m^3},$$

and the effective stagnation radius is taken as the nose radius of the model,

$$R_n = 0.04445\,\mathrm{m}.$$

The density-radius factor entering Eq. (11) is

$$\sqrt{\frac{\rho_\infty}{R_n}} = \sqrt{\frac{0.03116}{0.04445}} \approx 0.837.$$

Inserting these values into Eq. (11) with the Earth and Mars coefficients gives

$$\dot{q}_{c,\mathrm{E}} = k_{\mathrm{E}} \sqrt{\frac{\rho_\infty}{R_n}}\, V_\infty^3 \approx 1.7415 \times 10^{-4} \times 0.837 \times 3367^3 \approx 5.57 \times 10^6\,\mathrm{W/m^2} \approx 5.57 \times 10^2\,\mathrm{W/cm^2},$$

$$\dot{q}_{c,\mathrm{M}} = k_{\mathrm{M}} \sqrt{\frac{\rho_\infty}{R_n}}\, V_\infty^3 \approx 1.9027 \times 10^{-4} \times 0.837 \times 3367^3 \approx 6.08 \times 10^6\,\mathrm{W/m^2} \approx 6.08 \times 10^2\,\mathrm{W/cm^2}.$$

Thus, for shot 2254 with $R_n = 0.04445\,\mathrm{m}$, the Sutton-Graves correlation predicts stagnation convective heat fluxes of approximately

$$\dot{q}_{c,\mathrm{E}} \approx 5.6 \times 10^2\,\mathrm{W/cm^2}, \qquad \dot{q}_{c,\mathrm{M}} \approx 6.1 \times 10^2\,\mathrm{W/cm^2},$$

depending on whether the Earth air or Mars CO_2 coefficient is used. These values are roughly a factor of two smaller than the laminar super-catalytic Fay-Riddell and CFD stagnation point estimates ($\sim 1.1 \times 10^3\,\mathrm{W/cm^2}$) for the same case, reflecting the additional heating contribution from strong CO_2 dissociation and surface recombination captured by the more detailed models.

In summary, the Fay-Riddell model provides a high-fidelity laminar stagnation solution that can incorporate chemistry and wall catalysis explicitly, while the Sutton-Graves correlation offers a simple, widely used engineering estimate based only on ρ_∞, V_∞ and R_n. Together, these models form a robust baseline for comparison against CFD-predicted heating rates and for bounding uncertainties in trajectory analyses.

4.3. Detra-Kemp-Riddell / Detra-Hidalgo-Type Correlation

Besides Sutton-Graves, a widely used family of semi-empirical correlations for stagnation point convective heating originates from the work of Detra, Kemp and co-workers, later on generalized by Detra and Hidalgo [12]. These correlations were developed by fitting experimental and computational data over a broad range of hypersonic Earth entry trajectories and retain the same basic dimensional form as Sutton-Graves, but with a slightly different velocity exponent and coefficient. Although the correlation is not accurate for CO_2 reentries, one can try to predict the order of heat flux. A commonly used Detra-Hidalgo form for air entries can be written as

$$\dot{q}_{\mathrm{DH}} = K_{\mathrm{DH}} \left(\frac{\rho_\infty}{R_n} \right)^{1/2} V_\infty^{3.15}, \tag{12}$$

where $\dot{q}_{\mathrm{DH}}$ is the convective stagnation point heat flux in $\mathrm{W/m^2}$, R_n is the effective nose radius in m, ρ_∞ the freestream density in $\mathrm{kg/m^3}$, V_∞ the freestream velocity in m/s, and

$$K_{\mathrm{DH}} = 5.16 \times 10^{-5}$$

for the parameter ranges considered by Detra and Hidalgo [12] the exponent 3.15 on velocity reflects the slightly stronger-than-cubic dependence of the stagnation heat flux on V_∞ found in the data, compared to the pure V^3 scaling in Sutton-Graves.

In the present work, Eq. (12) is applied as an approximate engineering scaling for the CO_2 test case of shot 2254, with the understanding that the original Detra-Hidalgo calibration was performed in air and thus introduces some additional uncertainty for a pure CO_2 environment. Using the same freestream conditions and effective radius as for the Sutton-Graves evaluation,

$$V_\infty = 3367\,\mathrm{m/s}, \qquad \rho_\infty = 0.03116\,\mathrm{kg/m^3}, \qquad R_n = 0.04445\,\mathrm{m},$$

the density-radius factor becomes

$$\left(\frac{\rho_\infty}{R_n} \right)^{1/2} = \sqrt{\frac{0.03116}{0.04445}} \approx 0.837.$$

The velocity term may be expressed as

$$V_\infty^{3.15} \approx 4.3 \times 10^{10}\,\mathrm{m^{3.15}/s^{3.15}}.$$

Substituting into Eq. (12) provides

$$\dot{q}_{\mathrm{DH}} \approx 5.16 \times 10^{-5} \times 0.837 \times 4.3 \times 10^{10} \approx 5.6 \times 10^{6}\,\mathrm{W/m^2},$$

or, converted to W/cm^2,

$$\dot{q}_{\mathrm{DH}} \approx \frac{5.6 \times 10^6}{10^4} \approx 5.6 \times 10^2\,\mathrm{W/cm^2}.$$

For shot 2254 with $R_n = 0.04445\,\mathrm{m}$, the Detra-Hidalgo-type correlation therefore predicts a stagnation convective heat flux of about $5.6 \times 10^2\,\mathrm{W/cm^2}$, numerically very close to the Sutton-Graves Earth coefficient result and somewhat lower than the Sutton-Graves Mars coefficient. This is consistent with the similar structure of the correlations and reinforces the picture that classical air-based engineering formulas (Sutton-Graves and Detra-Hidalgo) cluster in the 5.5-6.0 $\times 10^2\,\mathrm{W/cm^2}$ range for this case, roughly half the laminar super-catalytic CFD value.

4.3.1. Summary of stagnation point Heating for Shot 2254

Table 4.1 summarizes the laminar stagnation point heat flux levels obtained for shot 2254 using the Fay-Riddell correlation, the Sutton-Graves and Detra-Hidalgo engineering correlations, and the laminar CFD results reported by Wright [1]. All values are referenced to the effective stagnation radius and the freestream conditions listed above.

Table 4.1. Shot 2254 laminar stagnation point heat flux estimates for different models and assumptions.

Model / correlation	Wall / chemistry assumption	$\dot{q}_w$ [W/cm^2]
Fay-Riddell	Equilibrium or frozen BL, fully catalytic, Le ≈ 1	$\approx 1.1 \times 10^3$
Sutton-Graves (Earth k_{E})	Air-based, fully catalytic $k_{\mathrm{E}} = 1.7415 \times 10^{-4}$	$\approx 5.6 \times 10^2$
Sutton-Graves (Mars k_{M})	Mars CO_2, fully catalytic $k_{\mathrm{M}} = 1.9027 \times 10^{-4}$	$\approx 6.1 \times 10^2$
Detra-Hidalgo type	Air-based $K_{\mathrm{DH}} = 5.16 \times 10^{-5}$, $V^{3.15}$ scaling	$\approx 5.6 \times 10^2$
DPLR CFD (Wright) [1]	Laminar, noncatalytic wall	$\approx 6.5 \times 10^2$
DPLR CFD (Wright) [1]	Laminar, Mitcheltree catalytic model	$\approx 7 \times 10^2$
DPLR CFD (Wright) [1]	Laminar, supercatalytic wall	$\approx 1.1 \times 10^3$

The present Fay-Riddell evaluation for shot 2254 yields a fully catalytic stagnation point heat flux of $\dot{q}_w \approx 1.1 \times 10^3\,\mathrm{W/cm^2}$, which is in excellent agreement with the laminar supercatalytic DPLR solution at the apex reported by Wright [1]. This level of agreement is very surprising although of a much appreciation, as Fay-Riddell is here applied with several simplifying assumptions (perfect-gas normal shock, ideal-gas CO_2 thermodynamics, Sutherland viscosity), yet it still reproduces the detailed CFD result to within the typical $\pm 10\%$ error band quoted for laminar reacting-gas heating in high-enthalpy CO_2 flows.

By contrast, the Sutton-Graves and Detra-Hidalgo correlations, which depend only on ρ_∞, V_∞, and R_n, predict stagnation convective heating in the range $\dot{q}_w \sim$ 5.6-6.1 $\times$ $10^2\,\mathrm{W/cm^2}$ for the same case, clustering just below the laminar noncatalytic DPLR stagnation heat flux of $\approx 6.5 \times 10^2\,\mathrm{W/cm^2}$ and well below the supercatalytic value. This behavior is consistent with their origin: Both Sutton-Graves and Detra-type formulas were calibrated primarily in air and collapse complex thermochemistry and surface catalysis into a single

fitted constant, without explicitly resolving CO dissociation $_2$ and finite-rate wall recombination. As a result, they provide reasonable noncatalytic-like estimates but underpredict the strongly catalytic heating measured and computed for high-enthalpy CO_2 flows.

Overall, the agreement with Wright's CFD is good in a bracketed sense: simple convective correlations together with the non-catalytic DPLR solution define a conservative lower bound on stagnation heating, while Fay-Riddell and the supercatalytic DPLR solution define a realistic upper bound for strongly catalytic CO_2 walls at high enthalpy.

5. Geometry Used in the Analysis

The stagnation-point heating analysis in this work is based on the 70° sphere-cone model tested by Wright in the T5 shock tunnel.[1] The forebody geometry is an axisymmetric 70° half-angle sphere-cone with a base diameter

$$D_b = 0.1778 \text{ m}, \qquad R_b = \frac{D_b}{2} = 0.0889 \text{ m},$$

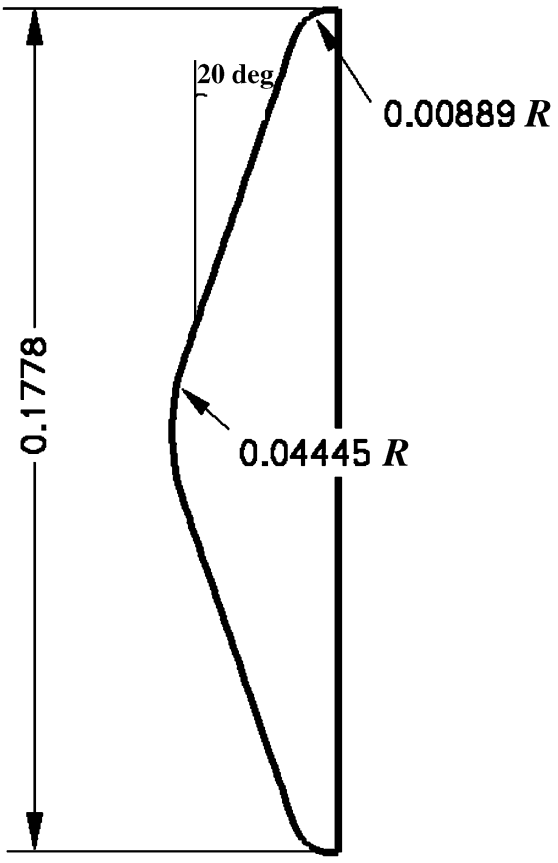
so that the model radius is $R_b = 0.0889$ m.[1] The spherical nose cap has the fixed radius,

$$R_n = 0.04445 \text{ m},$$

Figure 5.1 illustrates the geometry used in the analysis. The left panel shows a photograph of the stainless-steel 70° sphere-cone model mounted in the T5 facility, while the right panel shows the corresponding 2D meridional profile used for the present computations, adapted from Wright.[1]



(a) Photograph of the 70° sphere-cone scale model used in the T5 tests.



(b) 2D meridional view of the model geometry, adapted from Wright [1].

Figure 5.1. Geometry of the 70° sphere-cone model: (a) metal test article with thermocouple ports, (b) corresponding 2D profile used in the present analysis.

The test model also includes a finite shoulder radius blending the spherical nose to the conical part. Wright [1] note that this shoulder radius was chosen as approximately 10% of the base radius for manufacturing reasons, whereas the then-current MSL flight baseline used a shoulder radius of about 5% of the base radius.[1] Thus, the T5 model retains the canonical 70° sphere-cone nose shape and cone angle, but has a somewhat "softer" shoulder than the flight configuration.

The actual MSL aeroshell forebody is a full-scale spherically blunted 70° half-angle cone with a nominal heatshield diameter of 4.5 m, giving a base radius $R_b \approx 2.25$ m.

From the point of view of stagnation point aerothermodynamics, the most important geometric parameter is the nose radius R_n, which controls the local radius of curvature in the stagnation region and appears explicitly in the Sutton-Graves, Detra-Hidalgo and Fay-Riddell expressions. Because the T5 model and the MSL flight aeroshell use the same non-dimensional nose radius ratio $R_n/R_b = 0.5$, the stagnation-point heating levels and correlation trends obtained in this work are directly relevant to the full-scale MSL geometry, up to the usual differences in trajectory and freestream conditions. The larger shoulder radius of the T5 model primarily affects the heating distribution in the shoulder and leeside regions, but has negligible impact on the stagnation-point environment, which is governed by the local nose curvature and freestream parameters. Consequently, the stagnation point comparison between analytical correlations and DPLR CFD for shot 2254 provides a meaningful check on the fidelity of stagnation heating predictions despite the small geometric differences in the shoulder region.

6. Aerothermodynamics

During reentry conditions, extreme flow behaviour of hypersonic flight create multi-modal energy distributions where traditional perfect gas assumptions fail. Thus, the need for sophisticated models that account for vibrational excitation, chemical dissociation, and thermal non-equilibrium effects must be preserved. It is important to capture accurately the prediction of surface heating rates, shock layer structures and TPS performance during the reentry flight.

6.1. Energy modes and Heat Transfer

Movement of gas molecules can be expressed as the sum of components [13]: translational, rotational, vibrational, and electronic. As temperature rises, each of them gets more important and influences the flow more significantly. Each energy mode exhibits distinct characteristics in terms of energy level spacing and relaxation times, creating complex non-equilibrium behaviours under hypersonic conditions.

The first mode that occurs is the translational one, which describes the random movement of molecules in three-dimensional space. It is a mode which equilibrates in the most rapid way, as molecules collide with each other. The rotational energy mode, representing molecular rotation about axes perpendicular to the molecular bond, also equilibrates relatively quickly, particularly at lower temperatures where the energy level spacings are small compared to thermal energy.

Vibrational modes demand very high thermal energy to occur. Thus, they appear only in highly hypersonic flows and mainly in hypersonic shock layers with high temperatures. Vibrational excitation exhibits much longer relaxation times compared to translational and rotational modes.

The most energy-demanding excitation is the electronic one, as it becomes significant only at temperatures exceeding thousands of Kelvins. Energy modes involve the excitation of electrons to higher energy levels within atoms and molecules. Electronic excitation often precedes chemical dissociation and ionization processes, making it crucial for understanding the transition from molecular flow to plasma conditions in extreme hypersonic environments.

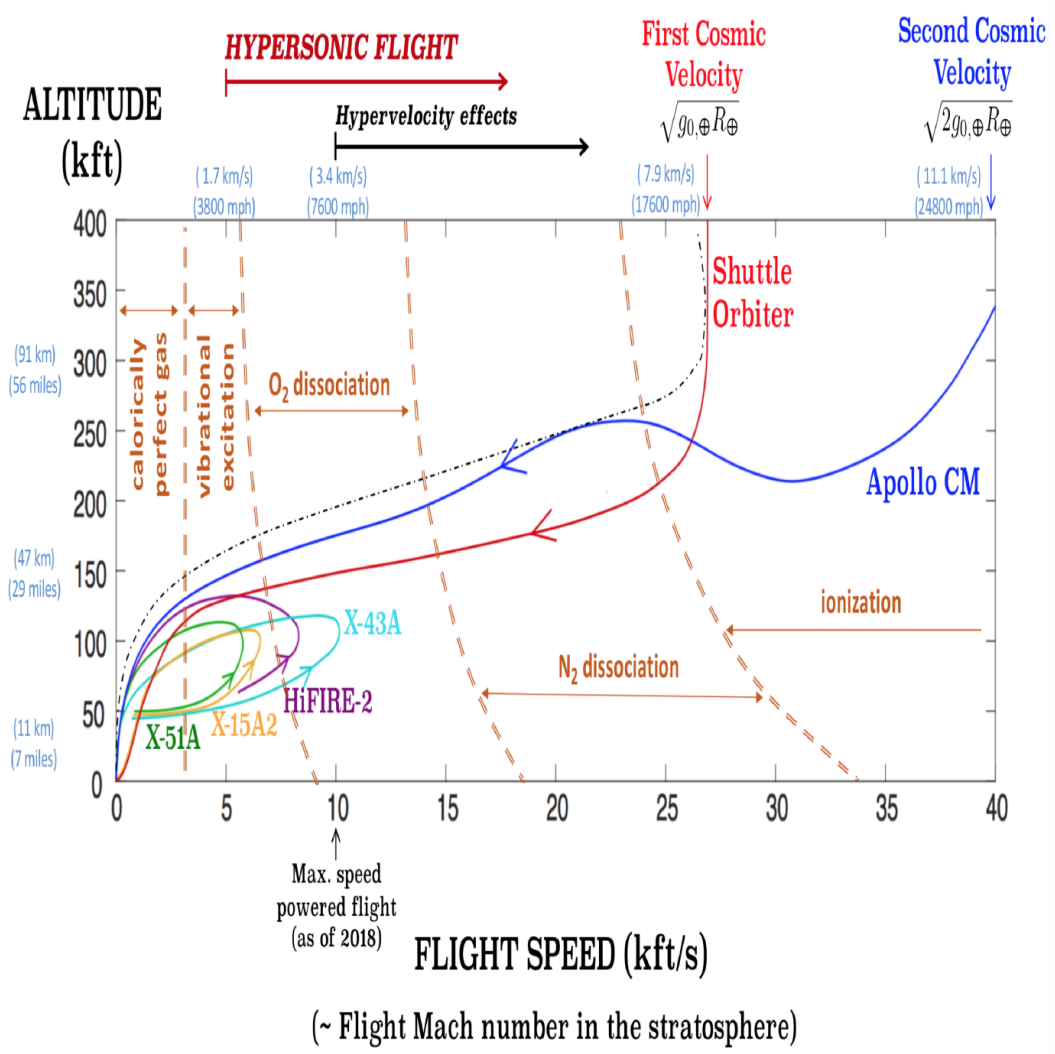


Figure 6.1. Illustrative flight trajectories of selected hypersonic vehicles and the approximate onset of vibrational excitation [13]

6.2. Radiation

In the present analysis, radiative heating is not considered as a separate contribution to the total heat flux. This simplification is justified because the entry regime investigated here is comparable to Earth-return conditions in which radiation is a secondary effect relative to convective heating. For example, the NASA study on EFT-1 reentry reported that radiative heating did not have a significant impact on either the total peak heat flux or the total heat load, although it was still relevant for detailed heating reconstruction [14]. Therefore, for the purpose of first-order aerothermodynamic modeling and TPS assessment, neglecting radiation is a reasonable approximation [14].

This assumption is also consistent with the general understanding that radiative heating becomes dominant only at much higher entry velocities and enthalpies, whereas for

moderate Earth-entry conditions the convective component remains the primary driver of surface heating [14].

6.3. Thermal Protection Systems

TPS are the thermal barrier between the external flow and the vehicle structure. They keep structural and component temperatures within limits during atmospheric entry or sustained high speed flight. For hypersonic vehicles, TPS concepts are usually grouped into four broad categories [15]: reusable insulative systems, ablative systems, semi-active concepts, and fully active cooling, each proper for a particular combination of entry speed, trajectory, ballistic coefficient, mission type, and reusability requirement.

Reusable insulative TPS manage heat primarily by limiting conduction into the structure and re-radiating part of the heat back into the flow. Typical examples include low-density silica or ceramic tiles and fibrous blankets (similar like on the Space Shuttle orbiters), together with more recent concepts based on ceramic-matrix-composite (CMC) [16] (6.2) hot structures that are both load-bearing and capable of operating at elevated surface temperatures. These systems are most appropriate for LEO crewed and cargo vehicles and for hypersonic cruise vehicles, where peak heat fluxes and integrated heat loads are moderate, the flight path is relatively shallow, and the vehicle must survive many reentries with manageable inspection and repair effort.



Figure 6.2. SPS CMC TPS array for thermal-mechanical testing [16]

Another type is ablative TPS, which in contrast, protect the structure by consuming material. The outer layer decomposes in process of pyrolysis and forms a char layer, and gradually recedes, when gases are being injected into the boundary layer providing additional protection by reducing convective heat transfer. This sacrificial behaviour makes ablators the preferred solution for high-enthalpy entries with large ballistic coefficients and significant uncertainty in laminar-turbulent transition, such as lunar-return capsules, Mars landers, and sample-return missions. Classical rigid charring ablators include AVCOAT and SLA-561V, while newer materials such as PICA (6.3) and its derivatives have been developed (6.4) to handle still higher heat fluxes and total heat loads [16].



Figure 6.3. Standard PICA model [16]



Figure 6.4. One of derivatives of PICA [16]

In the MSL mission, the forebody provides a representative example of a high-enthalpy ablative TPS [17]. The forebody of the MSL mission utilized a robust ablative TPS to endure entry, namely PICA developed by NASA's Ames Research Center [17]. The forebody heat shield material was the same as that used for the Stardust sample-return capsule and the SpaceX Dragon capsule, leveraging existing heritage for a demanding Mars entry trajectory [17]. A different approach was chosen for the rear side of the capsule, where the aeroheating levels are lower but still non-negligible: the backshell TPS employed the ablative but largely non-receding materials SLA-561V and Acusil-II, which behave more like high-temperature insulators for the aft-body environment [17]. Shock-tunnel and CFD studies, such as [1], were specifically conducted to resolve laminar and turbulent

heating on an MSL-class geometry and thereby reduce uncertainty in the environments used to size this ablative TPS.

Another, not so popular solution, is active TPS (6.5) that is using an external energy/mass source to remove heat from critical hot spots. Transpiration and film cooling strategies inject coolant gas through porous leading edges or along the surface, while regenerative cooling circulates cryogenic fuel through internal channels in sharp leading edges or engine inlets before combustion. These techniques are mainly considered for sharp edged hypersonic cruise vehicles and combined cycle propulsion systems, where local convective heat fluxes exceed the capability of both reusable and ablative passive TPS, and where aerodynamic performance constraints make blunt, highly radiative geometries impractical. Because active systems increase mechanical complexity and introduce new failure modes, their use is generally limited to small regions with extreme local heating or to sustained high-dynamic-pressure flight where no passive alternative is feasible.

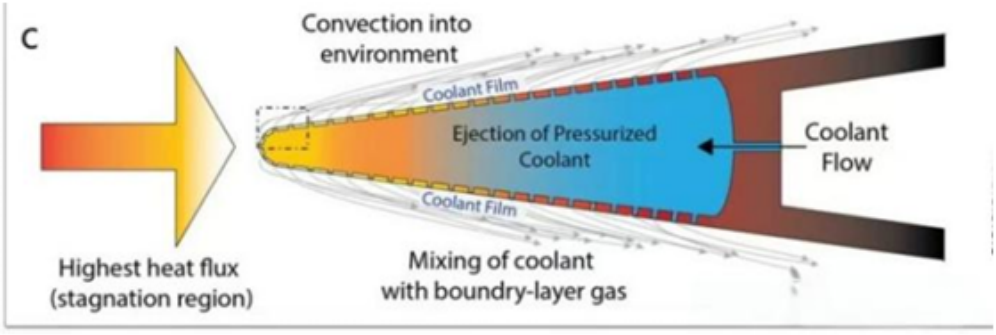


Figure 6.5. active TPS way of work [15]

Summing up, the choice of TPS concept for a hypersonic vehicle is justified by entry speed (thus by mission goal: LEO versus lunar or interplanetary reentry), atmospheric composition, ballistic coefficient and lift-to-drag ratio, mission type (crewed, cargo, or probe), reusability requirements, and allowable mass and risk. Reusable insulative TPS are favoured for LEO-class crewed and cargo vehicles with repeated shallow entries, while ablative systems such as PICA and AVCOAT are almost always adopted for high-enthalpy, high-β missions like MSL, Orion, and sample-return capsules. Semi-active and active TPS, together with advanced CMC hot structures and additively manufactured ablators, represent current and future directions aimed at enabling slender hypersonic cruise vehicles and very high-mass or outer-planet entries that lie beyond the capability of traditional TPS solutions.

If the heat flux experienced by an entry vehicle is insufficient to cause pyrolysis then the TPS material's conductivity could allow heat flux conduction into the TPS bondline material thus leading to TPS failure. Consequently, for entry trajectories causing lower heat flux, carbon phenolic is sometimes inappropriate and lower-density TPS materials such as the following examples can be better design choices.

One needs to remember that there is no universal TPS material that would fit all missions. A TPS material that is ideal for high heat flux may be too conductive for a long duration heat load. A low-density TPS material might lack the tensile strength to resist spallation if the dynamic pressure is too high. A TPS material can perform well for a specific peak heat flux, but fail catastrophically for the same peak heat flux if the wall pressure is significantly increased. Everything depends on mission profile and the trajectory which the spacecraft would follow.

7. Computational Fluid Dynamics

7.1. Governing Equation

One can define three equations that define the fundamental laws of fluid behaviour. They describe the conservation of mass, momentum and energy of a fluid. First of them, also called continuity equation [Eq. 13], says that mass cannot just vanish into thin air or appear from nowhere. In any fluid system, the mass flowing in must either flow out or accumulate, where this equation can be simplified for an incompressible flow [Eq. 14].

$$\frac{\delta \rho}{\delta t} + \nabla(\rho \vec{v}) = 0 \tag{13}$$

$$\nabla \cdot \vec{v} = 0 \tag{14}$$

The second equation defining conservation of momentum says that the rate of change of momentum equals the forces acting on the fluid. It is a form of Newton's second law for fluid mechanics. For compressible flows, it takes the form of [Eq. 15]. A common simplification in low-speed aerodynamics allows the use of an incompressible form of this equation, where viscosity can be assumed to be a constant value. Thus, the equation takes the form of [Eq. 16].

$$\rho\left(\frac{\partial \vec{v}}{\partial t} + (\vec{v} \cdot \nabla)\vec{v}\right) = -\nabla p + \nabla \cdot \boldsymbol{\tau} + \rho \vec{f} \tag{15}$$

$$\rho\left(\frac{\partial \vec{v}}{\partial t} + (\vec{v} \cdot \nabla)\vec{v}\right) = -\nabla p + \mu \nabla^2 \vec{v} + \rho \vec{f} \tag{16}$$

The third of the fundamental equations that define fluid mechanics is the energy equation. It describes how a fluid's total energy (including internal, kinetic, and sometimes potential energy) changes due to heat transfer, work done by pressure and viscous forces, and external body forces. It is the fluid-dynamics version of the First Law of Thermodynamics, governing how temperature and energy evolve within a flow. In compressible flow, the energy equation [Eq. 17] includes pressure work and compression heating, making it dependent on changes in density and internal energy, while in incompressible flow [Eq. 18], those terms drop out, reducing the equation to a heat transport equation driven by conduction and convection.

$$\frac{\partial}{\partial t}(\rho e_t) + \nabla \cdot (\rho e_t \vec{v}) = -\nabla \cdot \vec{q} + \nabla \cdot (\boldsymbol{\tau} \cdot \vec{v}) + \rho \vec{f} \cdot \vec{v} \tag{17}$$

$$\rho c_p \left(\frac{\partial T}{\partial t} + \vec{v} \cdot \nabla T\right) = k \nabla^2 T + \Phi \tag{18}$$

7.2. Turbulence Models

Because the Navier-Stokes equations for turbulent flows span a wide variety of spatial and temporal scales, their direct solution is computationally impossible in real-world computational fluid dynamics (CFD) applications. In order to address this issue, turbulence models are presented in order to approximate how the mean flow is affected by the unresolved turbulent fluctuations.

This can be accomplished by employing Reynolds averaging to separate the flow variables into mean and fluctuating components. Reynolds stresses, which indicate momentum transfer brought on by turbulence, are extra terms that emerge as a result of the process. These new terms cause the system to become unclosed, which is a problem known as the closure problem [18], because they add more unknowns than equations.

By expressing the Reynolds stresses in terms of known modeled quantities, like the eddy viscosity concept, turbulence models can be used to provide closure. It is done by using various turbulence models like Spallart-Almaras, k-ϵ, and k-ω to solve additional transport equations for turbulent properties, like turbulent kinetic energy, to approximate Reynolds stresses. This approach allows the modified Reynolds-averaged Navier-Stokes (RANS) equations to be solved efficiently for the mean flow field.

7.2.1. RANS

RANS approach is a numerical method that is based on decomposing flow quantities (like velocity and pressure) into their time-averaged and fluctuating components to model a turbulent flow. Most of these models are based on empirical observations.

$$u(x,t) = \overline{u}(x) + u'(x,t) \tag{19}$$

$$\overline{u} = \frac{1}{\Delta t}\int_{t}^{t+\Delta t} u_i \, dt \tag{20}$$

The governing equations for the mean flow variables are obtained by applying Reynolds averaging to the Navier-Stokes equations. But the momentum equation also contains other unknown terms, the Reynolds stresses, which need to be modeled in order to be closed. The momentum equation for incompressible flow looks like this:

$$\rho\left(\frac{\partial \overline{\vec{v}}}{\partial t} + \overline{\vec{v}}\cdot\nabla\overline{\vec{v}}\right) = -\nabla\overline{p} + \mu\nabla^2\overline{\vec{v}} - \nabla\cdot\left(\rho\,\overline{\vec{v}'\vec{v}'}\right) \tag{21}$$

The term $\rho\,\overline{\vec{v}'\vec{v}'}$ is called the Reynolds stress tensor, which must be modeled to close the system of equations. In order to do that, the Boussinesq approximation [19] is applied. It allows for modeling Reynolds stresses, as it introduces the concept of turbulent eddy viscosity μ_t.

$$-\rho\overline{v_i' v_j'} = \mu_t\left(\frac{\partial \overline{v}_i}{\partial x_j} + \frac{\partial \overline{v}_j}{\partial x_i}\right) - \frac{2}{3}\rho k\delta_{ij} \tag{22}$$

Here, $k = \frac{1}{2}\overline{v_i' v_i'}$ is the turbulent kinetic energy. This approximation enables the use of turbulence models to calculate μ_t.

Similarly, one can present RANS equations for compressible flow, as they differ from the incompressible ones. In compressible turbulent flows, the Reynolds averaging is applied to all flow variables, including density, velocity, pressure, and total energy. The Favre-averaging [20] technique is often used for thermodynamic variables, where a density-weighted average is applied. The decompositions are as follows:

$$\phi = \tilde{\phi} + \phi'', \quad \text{where} \quad \tilde{\phi} = \frac{\overline{\rho\phi}}{\overline{\rho}} \tag{23}$$

Here, $\tilde{\phi}$ represents the Favre-averaged variable, which can be any dependent variable and ϕ'' its fluctuation.

$$\frac{\partial(\overline{\rho}\tilde{\vec{v}})}{\partial t} + \nabla\cdot(\overline{\rho}\tilde{\vec{v}}\otimes\tilde{\vec{v}}) = -\nabla\overline{p} + \nabla\cdot\left[(\mu+\mu_t)\left(\nabla\tilde{\vec{v}} + \nabla\tilde{\vec{v}}^T - \frac{2}{3}\nabla\cdot\tilde{\vec{v}}\,\mathbb{I}\right)\right] \tag{24}$$

$$\frac{\partial(\overline{\rho}\tilde{e}_t)}{\partial t} + \nabla\cdot\left(\overline{\rho}\tilde{e}_t\tilde{\vec{v}}\right) = \nabla\cdot\left[(\lambda+\lambda_t)\nabla\tilde{T}\right] + \nabla\cdot\left[\tilde{\vec{v}}\cdot(\boldsymbol{\tau}+\boldsymbol{\tau}_t)\right] \tag{25}$$

Here, $\tilde{e}_t$ is the Favre-averaged total energy per unit mass, λ_t is the turbulent thermal conductivity, and $\boldsymbol{\tau}_t$ is the turbulent stress tensor derived using the eddy viscosity model.

$$\vec{q}_t = -\frac{\mu_t c_p}{Pr_t}\nabla\tilde{T} \tag{26}$$

7.2.2. SST k-ω Turbulence Model

The Shear Stress Transport (SST) k-ω model [21] combines the advantages of the k-ω model near walls with the k-ϵ model in the free stream. It uses blending functions to switch between these models based on distance from the wall and local flow properties. To model turbulent kinetic energy, the model uses Eq. (27) and for specific dissipation rate Eq. (28).

$$\frac{\partial(\rho k)}{\partial t} + \nabla\cdot(\rho k\vec{v}) = \nabla\cdot\left[\left(\mu+\sigma_k\mu_t\right)\nabla k\right] + P_k - \beta^*\rho k\omega \tag{27}$$

$$\frac{\partial(\rho\omega)}{\partial t} + \nabla\cdot(\rho\omega\vec{v}) = \nabla\cdot\left[\left(\mu+\sigma_\omega\mu_t\right)\nabla\omega\right] + \alpha\frac{\omega}{k}P_k - \beta\rho\omega^2 + 2(1-F_1)\frac{\rho\sigma_{\omega 2}}{\omega}\nabla k\cdot\nabla\omega \tag{28}$$

Here, F_1 is a blending function that activates the near-wall behaviour of the model. Constants like α, β, σ_k are typically calibrated based on experimental data for aerodynamic flows, but for most solvers, they are predefined and can be checked in manuals.

Due to the fact that Wright [1] describes turbulent and laminar models, and the case 2254 is laminar, one needs to describe the laminar turbulence model.

7.2.3. Laminar Model

The reference case analyzed in this work operates at given conditions, where the favorable pressure gradient across the windward forebody suppresses flow instabilities, maintaining a fully laminar boundary layer along the surface [1].

In contrast to the RANS formulation introduced in Section 8.2.1, a laminar model assumes the absence of turbulent velocity fluctuations ($u_i' = 0$, $\phi'' = 0$). Consequently, the Reynolds stress tensor vanishes:

$$-\rho\overline{v_i' v_j'} = 0, \quad \boldsymbol{\tau}_t = 0 \tag{29}$$

This implies that the turbulent eddy viscosity and turbulent thermal conductivity are zero:

$$\mu_t = 0, \quad \lambda_t = 0 \tag{30}$$

Additionally, the transport equations for turbulent kinetic energy k and specific dissipation rate ω (Eqs. 27 and 28) are deactivated, as $k = 0$ and $P_k = 0$.

Applying (30) directly simplifies the compressible momentum and energy transport equations back to their exact, not averaged continuum forms. The compressible momentum conservation equation reduces to:

$$\frac{\partial(\rho\vec{v})}{\partial t} + \nabla\cdot(\rho\vec{v}\otimes\vec{v}) = -\nabla p + \nabla\cdot\left[\mu\left(\nabla\vec{v} + \nabla\vec{v}^T - \frac{2}{3}\nabla\cdot\vec{v}\,\mathbb{I}\right)\right] \tag{31}$$

Similarly, the total energy equation simplifies as the turbulent heat flux vector $\vec{q}_t$ vanishes completely:

$$\frac{\partial(\rho e_t)}{\partial t} + \nabla\cdot\left(\rho e_t\vec{v}\right) = \nabla\cdot(\lambda\nabla T) + \nabla\cdot(\vec{v}\cdot\boldsymbol{\tau}) \tag{32}$$

where $\boldsymbol{\tau} = \mu\left(\nabla\vec{v} + \nabla\vec{v}^T - \frac{2}{3}\nabla\cdot\vec{v}\,\mathbb{I}\right)$ represents the purely molecular viscous stress tensor.

In high-enthalpy hypersonic flows, predicting surface heat transfer in the laminar regime relies entirely on accurate evaluation of molecular transport properties. Therefore, rather than relying on standard Sutherland approximations, molecular viscosity μ and thermal conductivity λ are evaluated using kinetic-theory-based formulations and NASA nine-coefficient polynomials. Adopting the laminar model for shot 2254 eliminates empirical turbulence closure uncertainties, allowing the numerical study to isolate the sensitivity of predicted heat fluxes to spatial discretization order, gas thermal nonequilibrium, and surface catalysis models.

7.3. Boundary Conditions

Setting proper boundary conditions is another crucial point, as it dramatically affects the solution. Boundary conditions set for inlet used the most often in external aerodynamics are velocity inlet and pressure far-field, depending what is the goal of the simulation. To simplify this case, the axisymmetric BC will also be analyzed. Besides wall BC, there will be also pressure-outlet boundary condition, which is an usual approach in external aerodynamics.

7.3.1. Pressure Far-Field

The pressure far-field boundary condition is applicable only in certain situations. It may be used solely when the gas density is evaluated via the ideal-gas law and when the outer boundary is placed sufficiently far from the body (for an airfoil, a distance of about 20 chord lengths is a standard). In addition, it is not compatible with constant-density flows, real-gas models, or wet-steam models, all of which are usable with the density-based solver. A further restriction is that this boundary condition cannot be combined with the multiphase models available in the pressure-based solver [22].

In contrast to incompressible flows, where pressure satisfies an elliptic behavior and disturbances in pressure are communicated instantaneously across the entire domain, compressible flows obey hyperbolic conservation laws. This essential distinction imposes both mathematical and physical limits on which boundary conditions are permissible and on the manner in which they must be specified.

Mass conservation

The conservation of mass is governed by the continuity equation:

$$\frac{\partial \rho}{\partial t} + \frac{\partial (\rho u)}{\partial x} = 0. \tag{33}$$

Momentum conservation

The momentum density is describe by the term ρu, and the momentum flux consists of two parts: convective transport and pressure effects. The convective momentum flux is denoted as ρu^2. The pressure p arises from molecular motion and contributes to the momentum flux. Hence, the momentum conservation equation is:

$$\frac{\partial (\rho u)}{\partial t} + \frac{\partial}{\partial x}\left(\rho u^2 + p\right) = 0. \tag{34}$$

Energy conservation

The total energy consists of internal energy density ρe and kinetic energy density $\frac{1}{2}\rho u^2$:

$$E = \rho e + \frac{1}{2}\rho u^2. \tag{35}$$

The energy flux has contributions from bulk motion and pressure work, yielding the conservation of energy equation:

$$\frac{\partial E}{\partial t} + \frac{\partial}{\partial x}\big(u(E+p)\big) = 0. \tag{36}$$

7.3.2. Velocity inlet

While the pressure far-field boundary condition is the formally correct choice for modeling external compressible flows, in practice it demands large computational domain that can become impractical for large-scale problems or simulations with limited resources. On the other hand, the velocity inlet boundary condition offers substantial practical benefits for simulations using more compact computational domains, especially in hypersonic flow studies where the main physical phenomena of interest occur near the body and far-field influences are of secondary importance.

In the present study [1], a velocity inlet boundary condition was applied to the computational domain. The shock tunnel nozzle exit provides known inflow conditions (velocity, temperature) that are uniform across the core of the test section. By adopting the velocity inlet condition, the computational domain is restricted to the test section and the shock-interaction region surrounding the model, providing acceptable computational resources used, while preserving accuracy in the main area of interest.

The mass flow rate entering a fluid cell adjacent to a velocity inlet boundary is computed from the specified velocity components normal to the control volume face (Eq. 37) where only the velocity component normal to the control volume face contributes to the inlet mass flow rate. This calculation demonstrates that specifying velocity directly determines the mass flow rate entering the domain, which is then used by the continuity equation to constrain the interior solution.

$$\dot{m} = \rho\, u_n\, A \tag{37}$$

7.3.3. Pressure outlet

The pressure outlet boundary condition is used to specify the static pressure at domain exit boundaries while allowing velocity and density to be determined by the interior flow solution.

The pressure outlet requires specification of backflow conditions (total pressure and temperature) as a safeguard in case flow reverses and enters the domain through the outlet boundary during iteration. In well modeled simulations, such backflow should not occur, but the specification prevents solver instability if it does in our case.

For shock tunnel aeroheating analysis, the pressure outlet is the best specification because the test section exhaust flow is subsonic after shock-induced deceleration, and the ambient pressure environment is known and precisely controllable. Combined with velocity inlet, this pressure outlet BC pairing represents the standard configuration for

internal compressible flows and is well-suited to shock tunnel geometry where both inlet conditions and outlet conditions are experimentally characterized and known.

7.3.4. Symmetry

Symmetry boundary conditions are used when the physical geometry of interest and the expected pattern of the flow and solution have mirror symmetry. The primary advantage of symmetry boundaries is the reduction of computational domain size: if geometry and flow are symmetric about a plane, only half (or a smaller fraction) of the domain needs to be modeled, significantly reducing mesh size and computation time. There are several limitations of this approach [23], as there is no flow penetration across the symmetry plane [Eq.38] and gradient of all flow variables including velocity components, pressure, temperature, turbulence quantities, and species mass fractions is zero [Eq. 39].

$$u_n = 0, \tag{38}$$

$$\frac{\partial \phi}{\partial n} = 0 \tag{39}$$

For shock tunnel aeroheating analysis [1] at zero angle of attack, the axisymmetric case is justified because it is expected to obtain a solution that is invariant across any symmetry plane containing the body axis. The laminar character of shot 2254 (low Reynolds number) and absence of turbulent transition ensures perfect maintenance of symmetry throughout the solution domain. The pressure field, velocity field, and temperature distribution all exhibit complete axisymmetry, validating the use of half-domain symmetry reduction.

Besides geometry symmetry, there is a need to distingouish whether the flow will be symmetric itself, as symmetry boundaries should be applied only when both the geometry and the expected flow pattern are truly symmetric. There are important cases where symmetry would be inappropriate despite geometric symmetry. When buoyancy forces create density-driven circulation, the resulting flow may be asymmetric even though geometry is symmetric. Similarly, if swirl or rotational velocity exists in the flow, the flow is no longer symmetric about the axis and cannot be modeled with symmetry conditions.

7.4. Boundary Layer

The next quantity that needs to be observed is y^+. For turbulence models such as the SST $k-\omega$ model, maintaining $y^+ \approx 1$ for the first cell adjacent to the wall ensures that the viscous sublayer is directly resolved, although values up to 5 are acceptable. This is essential for capturing the near-wall flow dynamics of viscous flows and accurately predicting surface heat and velocity boundary layers [7.1]. Depending on the choice of turbulence model, one needs to adjust the y^+ value and wall functions.

$$y^+ = \frac{\rho u_\tau y}{\mu} \tag{40}$$

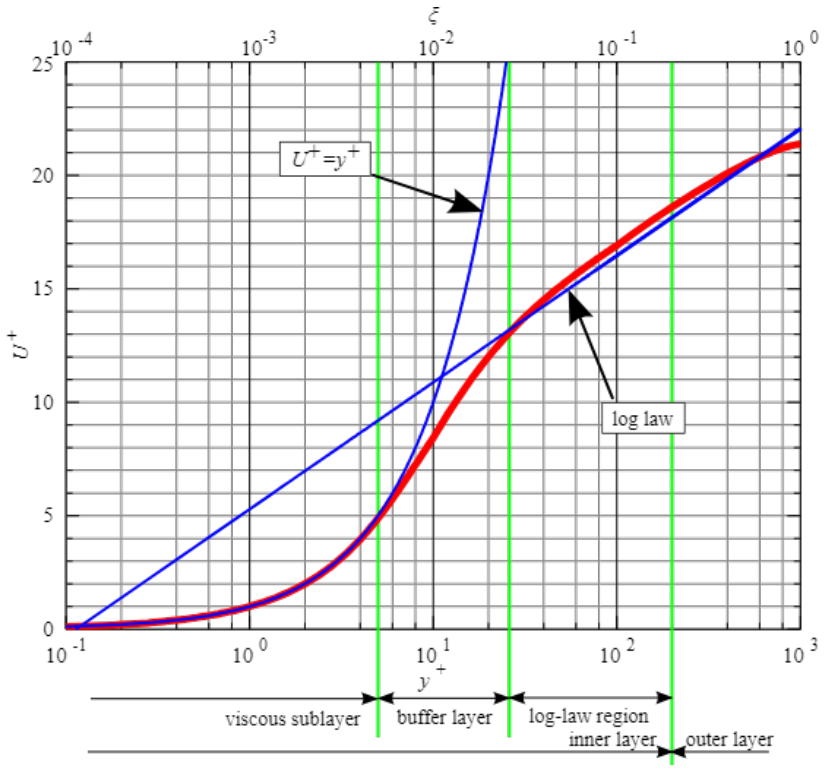


Figure 7.1. Boundary Layer subdivisions [5]

Although this approach is correct for most CFD cases, it may fail for highly hypersonic regimes, as it assumes constant fluid properties and a fully developed boundary layer. In analysed flows such assumptions break down due to multiple factors: steep property gradients as near-wall regions exhibit extreme temperature-dependent viscosity (μ) and density (ρ) variations, thermo-chemical nonequilibrium leading to dissociation and ionisation altering boundary layer thickness and heat flux, which leads to rendering y^+ based on frozen chemistry invalid. More accurate quantity, which is reliable in hypersonic regimes, is semi local wall coordinate y^*

$$y^* = \frac{y \cdot \rho u_\tau^*}{\mu} \tag{41}$$

Some of the studies have shown that y^* better correlates with laminar-turbulent transition onset in hypersonic boundary layers [24] and maintains accuracy when vibrational excitation and dissociation dominate [24]. Studies confirmed that in DNS, y^+ may overpredict the thickness of near-wall regions by up to 300% at M=8 [25]. Another source informs that y^+ fails when $\frac{\mu_{wall}}{\mu_\infty} > 10^3$ [26].

Due to the complexity of highly hypersonic flow, there is a need to influence another important parameter to observe: Re_{cell}. The general rule is to keep it below 1, as it is

known to stabilise the numerical solution across shock-induced separation bubbles. This is a second order parameter, which should be modeled by adaptive meshing later on in gradient-rich regions [24].

Ommiting any of the criteria of these two parameters caused premature transition predictions and overestimated heat flux peaks by 40-60% [24]. Another important influence of these quantities is that the study reported that violating these criteria in Orion capsule simulations led to non-physical separation bubble growth and 15-20% underprediction of heat loads on windward surfaces.

7.5. Fluid Mixture Model

The temperature at the bow shock reaches thousands of Kelvins during the hypersonic velocities. As it happens, a noticeable part of the flow is in thermal and chemical nonequilibrium. In addition, flow is considered to be significantly affected by high enthalpy effects and dissociates into atomic species [27]. For hypersonic reentry physics, it is important to capture all the effects present during this phenomenon, such as heating of the gas, ionization and dissociation. They are of much importance when modeling the flow, as they directly influence heat flux and pressure distributions of the spacecraft.

To capture all possible species in the environment, the pre-defined Fluent database defining mars-11-species would be the best approach to be used, as it is known to be precise at aerothermodynamics of hypersonic flows reaching thousands of Kelvins. Although this model would fit the analysed case the best, it is computationally expensive due to the number of chemical species present in it.

Due to the limited computational power, ionisation effects were omitted in further analysis, and the mars-5-species was chosen, where the only difference between them is the lack of ionisation effect components. This model is still viable in hypersonic flows to be used with simulation of temperatures reaching up to $\approx$ 8000K, and is also capable of accounting for nonequilibrium effects by solving separate energy equations for translational-rotational and vibrational-electronic modes, but may not capture all vibrational-electronic interactions accurately at extreme conditions.

8. Mesh Sensitivity

Avoiding errors is crucial in CFD, as even small discrepancies can lead to significantly different simulation outcomes, ultimately impacting design decisions and performance predictions. Errors can be categorised into subcategories [28]:

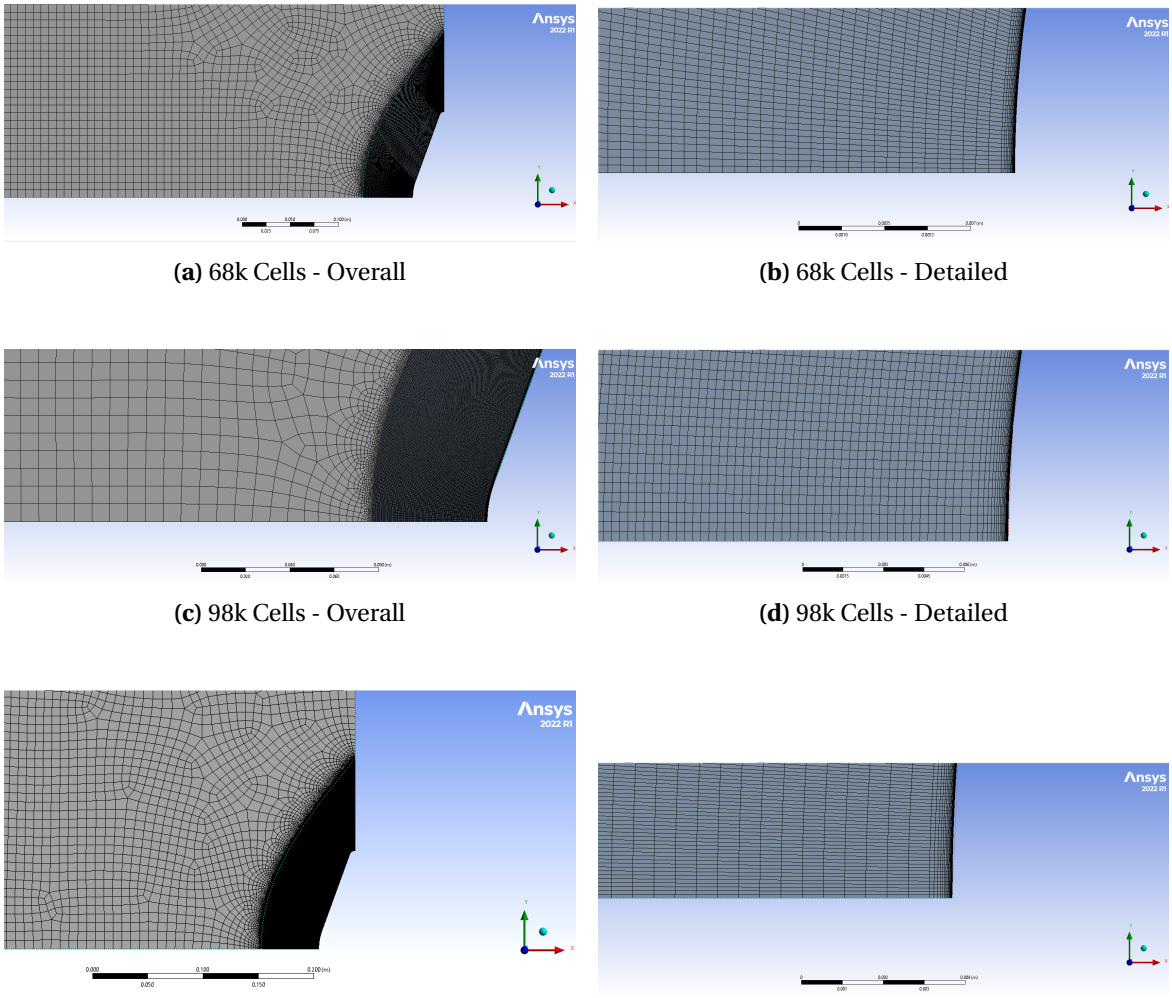
- Acknowledged Errors
  - Physical approximation error: These arise from simplifications in the governing equations and turbulence models, or from uncertainties in input parameters.
    - Physical modeling error
    - Geometry modeling error
  - Computer round-off error: Caused by the finite precision of floating point arithmetic.
  - Iterative convergence error: Occurs when iterative solution methods stop before achieving the true solution.
  - Discretisation error: Result from representing continuous equations on a discrete grid, which includes both spatial and temporal discretisation errors.
    - Spatial discretisation error
    - Temporal discretisation error
- Unacknowledged Errors
  - Computer Programming Errors: Bugs or flaws in the code.
  - Usage Errors: Mistakes in setting up simulations, such as improper boundary conditions or solver settings.

Among these, discretisation error is particularly significant because it directly depends on the quality and resolution of the computational mesh. Mesh sensitivity studies offer a systematic way to reduce discretisation error. By refining the mesh and examining the convergence of key solution parameters, one can ensure that the numerical solution is less influenced by discretisation and more representative of the true physical behavior.

Mesh sensitivity studies were conducted on a similar to the final ones conditions (8.2). Multiple different mesh resolutions were generated to assess whether the discretisation error had been minimised. Although the primary objective was to evaluate the heat flux of the surface, the convergence of heat flux takes greater ammount of iterations to stabilise, thus the drag coefficient was chosen for the mesh check (8.1).

Mesh	elements (x1000)	c_d	max skewness
1	68	1.5976	0.75
2	98	1.5975	0.72
3	184	1.6089	0.71
4	312	1.6107	0.84
5	796	1.6100	0.9

Table 8.1. Mesh Sensitivity Study Data



(a) 68k Cells - Overall

(b) 68k Cells - Detailed

(c) 98k Cells - Overall

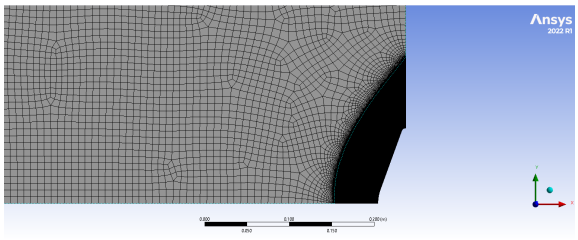
(d) 98k Cells - Detailed

(e) 184k Cells - Overall

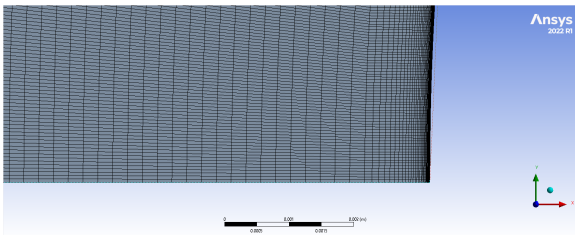
(f) 184k Cells - Detailed

Figure 8.1. Mesh sensitivity study showing overall grid domain and boundary layer close-ups (Part 1).

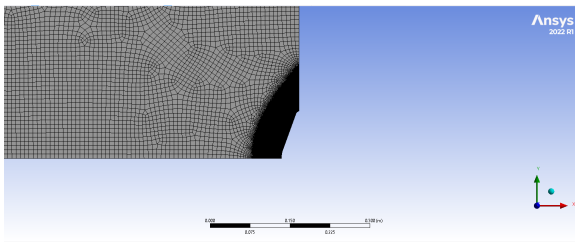
The computational grid parameters were being refined, with a primary focus on the close to the body region. The specific modifications consisted of the local cell dimensions, the total number of inflation layers, the first-layer thickness, and the growth rate of these boundary layers. Accurately defining these settings is essential for generating a fine mesh



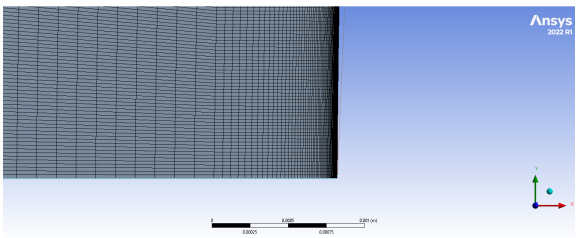
(g) 312k Cells - Overall



(h) 312k Cells - Detailed



(i) 796k Cells - Overall



(j) 796k Cells - Detailed

Figure 8.1. Mesh sensitivity study showing overall grid domain and boundary layer close-ups (Part 2).

capable of working with stable and physically correct numerical solutions. Furthermore, the boundary layer growth rate is a particularly critical parameter in aerodynamic heating and convective heat transfer analyses, as it dictates the solver's ability to accurately capture the steep thermal gradients adjacent to the vehicle surface.

Based on the mesh sensitivity study results presented in Table 8.1, Mesh 3 was selected for all subsequent simulations. The drag coefficient between Mesh 3 and Mesh 4 is sufficiently converged, with only a 0.1% difference , providing sufficient criteria to state that grid independence has been achieved. Although Mesh 4 and Mesh 5 show improvements in solution accuracy, they introduce much higher computational costs. Coarser meshes (Mesh 1 and 2) exhibit insufficient convergence in the drag coefficient, suggesting unresolved flow features, like shockwave. Therefore, Mesh 3 represents the optimal balance between solution accuracy, mesh quality, and computational efficiency for the subsequent heat flux analysis and aerodynamic studies.

Parameter	Value	Unit
Velocity	3000	m/s
Temperature	1828	K
Pressure	13670	Pa
Turbulence Model	Laminar	—
Reference Area	0.024816	m^2

Table 8.2. Mesh Sensitivity Simulation Settings

8.1. Mesh

8.1.1. SST k-ω

The previously chosen mesh was created following the rules of creating a proper mesh for the SST k-ω model, such as a sufficiently large computational domain, proper orthogonal quality, skewness, AR, y^+, and a carefully modeled boundary layer.

An orthogonal mesh, where the cell faces meet at near 90° angles, is preferred as it reduces numerical diffusion and improves solution stability. The orthogonal quality of the mesh is evaluated by checking that the angles between grid lines are maintained close to 90°, as deviations can lead to inaccuracies in the computed gradients. Values closer to 1 indicate good orthogonal quality mesh, and values near 0 indicate bad cells. The general rule is to keep orthogonal quality greater than 0.15 for all cells and an average value greater than 0.35. For some cases, it is acceptable to use a minimum value of orthogonal quality greater than 0.05, and the critical value for Ansys Fluent to solve the simulation properly without any initial errors is 0.01.

The aspect ratio of the cells, defined as the ratio of the longest to the shortest dimension of an element, is another critical parameter. Excessively high aspect ratios, particularly in regions with strong gradients, can distort the representation of flow features and lead to numerical instability, particularly in the subject of heat transfer. Therefore, it is imperative to control the AR, especially in critical regions near the vehicle surface and in the wake.

Cell skewness is also an important measure of mesh quality. Skewness quantifies the deviation of a cell from an ideal shape. Low values of skewness are desirable because high skewness can adversely affect the accuracy of gradient approximations and, consequently, the overall solution quality. The rule in the industry is to keep skewness below 0.9 [29] with as small an average value as possible. For skewness cells greater than 0.98, the Fluent grid check may fail [30].

Another quantity is y^+ value, which for the chosen model should be approximately equal 1. Assuring this allows a direct solve of a viscous layer in a boundary layer, which for reentry conditions tends to be the most reliable approach from two-equation models.

When applying this turbulence model, it is important to consider some extra meshing factors. The model reacts strongly to how well the mesh is set up near the walls, so a finer mesh is needed in areas where the boundary layer forms. On the other hand, areas that are far from the wall, like the free stream and parts of the wake, do not need such a detailed mesh. This means one can use a coarser mesh there to save on computing power while still keeping accuracy. Often, adaptive meshing techniques are used to make sure that regions with expected high gradients - like where shocks happen, flow separates, or where there are quick changes in thermal flux - are refined enough to accurately represent the flow behaviour.

Furthermore, special attention must be paid to regions where the SST k-ω model is most sensitive while allowing insignificant areas to be meshed more coarsely. Ensuring

these conditions not only brings up the accuracy of the simulation but also increases the reliability of the predictions.

8.2. Computational Settings

As already stated, this thesis focuses on case 2254 in Wright's article [1], thus the following conditions were chosen for calculations. Temperature of the front wall and chamfer was set to 300K, as it is stated in the article. The only not known value from the article is freestream pressure, which needs to be calculated.

$$M_{CO_2} = 44.01 \text{ g/mol} = 0.04401 \text{ kg/mol} \tag{42}$$

The specific gas constant is obtained from the universal gas constant divided by the molecular weight:

$$R_{\text{specific}} = \frac{R_{\text{universal}}}{M_{CO_2}} \tag{43}$$

where:

$$R_{\text{universal}} = 8.314 \text{ J/(mol} \cdot \text{K)} \tag{44}$$

$$M_{CO_2} = 0.04401 \text{ kg/mol} \tag{45}$$

Substituting:

$$R_{\text{specific}} = \frac{8.314}{0.04401} = 188.91 \text{ J/(kg} \cdot \text{K)} \tag{46}$$

For an ideal gas, the relationship between pressure, density, and temperature is:

$$p = \rho \, R_{\text{specific}} \, T \tag{47}$$

Applying this to freestream conditions:

$$p_\infty = \rho_\infty \, R_{\text{specific}} \, T_\infty \tag{48}$$

Substituting the numerical values:

$$p_\infty == 0.03116 \text{ kg/m}^3 \times 188.91 \text{ J/(kg} \cdot \text{K)} \times 1828(K) = 10760.50 \text{ Pa} \tag{49}$$

Pressure expansion ratio from stagnation to static conditions:

$$\frac{p_\infty}{p_0} = \frac{10760.50}{19.45 \times 10^6} = 5.53 \times 10^{-4} \approx \frac{1}{1808} \tag{50}$$

This huge pressure drop is typical of shock tunnel nozzle expansions used to generate hypersonic, low-pressure flows representative of planetary entry conditions, which is a trustworthy result.

9. Solver

Computational calculations are conducted using ANSYS Fluent v2022R01 software, which is a dedicated program for performing CFD calculations.

9.1. Compressibility Models

In order to determine what modeling approach would be preferable in this analysis, there is a need to check in which Mach regime the flow is. Knowing the speed of sound in the environment [Eq. 51], one can calcualate Mach number of the freestream flow [Eq. 52].

$$a = \sqrt{\gamma RT} = \sqrt{1.29 \cdot 188.91 \frac{J}{kg \cdot K} \cdot 1828K} = 667.44 \frac{m}{s} \tag{51}$$

$$M = \frac{3367 \frac{m}{s}}{667.44 \frac{m}{s}} = 5.045 \tag{52}$$

Mach number indicates, that the flow is hypersonic, thus compressibility effects are present and should be taken into account in simulations. This leads to the conclusion, that density-based model should be used in further runs.

9.2. Energy equation and modes of motion

The energy equation is solved explicitly in all simulations to capture the temperature field and heat transfer to the aeroshell surface. In hypersonic flow, compressibility effects couple kinetic energy directly into thermal energy through shock waves and viscous dissipation, making the energy equation inseparable from the momentum and continuity equations. Without solving the energy equation, the temperature field cannot be determined, and therefore the convective heat flux to the wall, defined as equation [Eq. 53], cannot be computed.

$$q = -k(\frac{dT}{dy})|_{wall} \tag{53}$$

Since the primary quantity of interest in this study is the aerothermal heating rate on the aeroshell, activation of the energy equation is mandatory. Additionally, the energy equation is required to capture the large temperature variations across the shock layer (from approximately 1828 K in the freestream to 300 K at the wall, and thousands of Kelvins in the shockwave), which directly influence the transport properties and hence the overall flowfield behavior.

In the Wright [1] all CO_2 shots, including case 2254, are analysed using Park's two temperature (2T) formulation to account for thermal nonequilibrium between translational-rotational and vibrational energy modes in the post shock mixture. In this model, one temperature

represents the translational-rotational energy of the heavy particles, while a second temperature represents the vibrational energy; vibrational modes are in equilibrium with each other but not necessarily with the translational-rotational modes. Chemical source terms are evaluated using an effective control temperature derived from both, so that vibrational excitation can accelerate dissociation compared with a single-temperature perfect-gas assumption [31].

For the present CFD, the same 2T approach is adopted as in Wright's study [1], to ensure consistency between the tunnel data analysis and the flight-environment predictions. Although the authors note that, for the T5 CO_2 conditions, the degree of thermal nonequilibrium is relatively small due to fast CO_2 vibrational relaxation, the 2T model is still important: it allows the simulation to capture any residual separation between translational and vibrational temperatures in the shock layer, and hence to represent more accurately the post-shock temperature field, species distributions, and wall heat flux used to calibrate catalysis models and validate the aeroheating predictions for MSL [32].

9.3. Species

In the hypersonic simmulation it is important to remember that high speed flows require species transport to be modeled, as mentioned in the section 2.3. This need comes from the fact that it plays a crucial role in capturing the behaviour of multicomponent gases and their interactions under extreme temperatures. Moreover, this apprach allows for the simulation of multicomponent gas mixing and has ability of defining and tracking dissociation reactions.

The transport of species in CFD simulations enables the monitoring of various gas species as they interact, mix, and participate in chemical reactions throughout the high speed flows. In the context of hypersonic flows, dissociation reactions are vital for precise predictions of aerodynamic heating and the chemical composition of the flow. Such reactions are crucial for accurately representing the thermochemical characteristics of the flow near the surface of the reentry vehicle.

In high temperature environments, reactions occur in the bulk of the gas phase, referred to as volumetric reactions. The species model in Fluent handles these reactions, including air dissociation models, effectively capturing the chemical processes that influence flow properties such as density, temperature, and viscosity.

The freestream condition for all three cases is a high enthalpy CO_2 flow representative of MSL entry, and the gas in the shock layer is treated as a reacting CO_2-CO-O_2-O mixture. In contrast to a single-species perfect-gas approximation, solving separate conservation equations for species ensures that the computed aeroheating is consistent with the real-gas behaviour observed in the experiments.

The interaction between the gas composition and the aeroshell surface is modeled

through catalytic wall boundary conditions that represent recombination of dissociated species at the wall.

9.4. Freestream Gas Model

The present study analyses a laminar zero AoA case from Wright [1], with freestream conditions given in Table 2 of the article. These represent a high-enthalpy CO_2 flow designed to simulate MSL entry environments. The freestream properties are computed from measured reservoir conditions using nozzle expansion calculations that include finite rate chemistry and Park's 2T nonequilibrium model, ensuring consistency with the real-gas physics in the T5 facility. Note that the stagnation pressure p_0 in Table 2 is the nozzle throat stagnation pressure, which sets the freestream density and Reynolds number for the test model 9.1.

Table 2 Shot matrix and computed freestream conditions for the test series

Shot #	h_0 (MJ/kg)	p_0 (MPa)	α (deg)	u_∞ (m/s)	ρ_∞ (kg/m^3)	T_∞ (K)	c[CO_2]	c[O_2]	c[CO]	c[O]
2254	10.6	19.45	0	3367	0.03116	1828	0.55	0.151	0.287	0.012

Figure 9.1. Freestream 2254 shot conditions

For the reference case of shot 2254, Table 2 (9.1) lists a total enthalpy $h_0 = 10.6$ MJ/kg, stagnation pressure in tunnel $p_0 = 19.45$ MPa, freestream velocity $u_1 = 3367$ m/s, density $\rho_1 = 0.03116$ kg/m^3, and temperature $T_1 = 1828$ K. The species mass fractions are $c_{CO2} = 0.55$, $c_{O2} = 0.151$, $c_{CO} = 0.287$, and $c_O = 0.012$, reflecting partial dissociation from reservoir chemistry and nozzle expansion. Wright [1] notes that flow properties vary by less than 3% across the 20 cm nozzle core, justifying a uniform freestream in the CFD.

These conditions are applied directly at the CFD inflow, using the reacting CO_2-CO-O_2-O mixture and 2T as in the original study. This approach captures the thermochemically nonequilibrium inflow that determines shock strength, post-shock dissociation, and wall heat transfer on the MSL forebody model.

In order to simulate the present conditions as accurately as possible, it is necessary to specify appropriate material properties for the gas. In the thesis, the most important thermophysical parameters are the specific heat, viscosity, and thermal conductivity, as they directly influence the predicted temperature field and surface heat flux. The specific heat is evaluated using NASA's nine-coefficient piecewise polynomial fits, which are widely used in high temperature gas and combustion modeling and provide an accurate representation of $c_p(T)$ over a broad temperature range.

Because the focus of this thesis is on the overall laminar behaviour of the flowfield rather than on detailed turbulence modeling, viscosity and thermal conductivity are computed using expressions derived from kinetic theory rather than more exact engineering correlations. Classical Sutherland type laws, which are calibrated for moderate temperatures, are known to lose accuracy under high-enthalpy conditions and can underpredict

transport coefficients at these temperatures. Adopting a kinetic theory based formulation therefore ensures a more reliable description of viscous and conductive transport in the high temperature regime relevant to the present analysis, without introducing unnecessary complexity into the laminar simulations.

10. Computational Domain

The numerical simulations in this thesis are based on a 70° sphere-cone geometry representative of MSL forebody, matching the model tested in the T5 reflected shock tunnel. The configuration consists of a spherical nose smoothly blended into a conical frustum, with dimensions scaled to the 5% wind-tunnel model used in the experimental campaign. This idealised, axisymmetric shape captures the essential aerothermal features of the MSL aeroshell while remaining sufficiently simple to enable systematic variation of CFD modeling parameters.

To reproduce the T5 test environment, the model is placed in a two dimensional axisymmetric computational domain extending several nose radii upstream, downstream and sideways. The domain is concentrated on the forebody region to ensure high-fidelity capture of stagnation-point aeroheating while maintaining computational efficiency. The outer boundaries are located far enough from the body to avoid interaction with the bow shock and to permit the imposition of uniform freestream conditions corresponding to shot 2254. The overall layout of the geometry and computational domain is illustrated in Fig. 10.1.

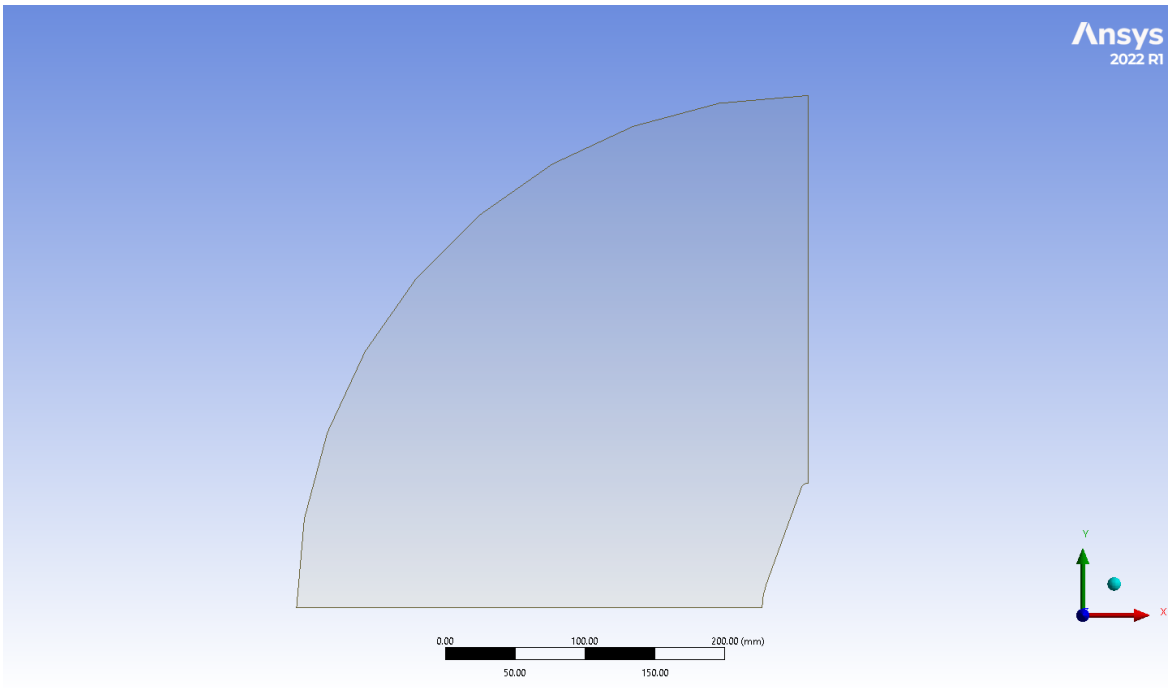


Figure 10.1. Computational domain used in the simulations.

11. Results

The numerical results are organised to separate numerical effects from physical modeling choices (wall catalysis and thermal nonequilibrium). All simulations are based on the shot 2254 freestream conditions. To keep the notation compact, each configuration is labelled as:

$$\texttt{X-Y-Z},$$

where:

- $\texttt{X} \in \{\texttt{A},\texttt{B},\texttt{C},\texttt{D}\}$ identifies the wall model (no heat flux, non-catalytic, supercatalytic, Mitcheltree),
- $\texttt{Y} \in \{\texttt{FS},\texttt{SS}\}$ denotes the spatial scheme: First-order Scheme, Second-order Scheme,
- $\texttt{Z} \in \{\texttt{1T},\texttt{2T}\}$ denotes the gas thermal model: single-temperature, two-temperature.

11.1. Definition of Case Families

Four base case families are defined by the wall boundary condition; within each family, four numerical/thermal variants are considered:

The naming convention for the simulations is defined by the wall boundary condition and the specific numerical discretization settings applied and thermal mdoel. The simulations are grouped into four primary families based on the wall-chemistry treatment: Family A assumes an adiabatic wall with no heat flux, Family B is a non-catalytic wall, Family C models a supercatalytic wall that forces full recombination, and Family D applies the Mitcheltree surface reaction model. Within each family, specific numerical and gas models are denoted by a set of abbreviations. The spatial discretization is indicated by either FS for a first-order scheme or SS for a second-order scheme. Additionally, the thermal treatment of the gas is denoted by 1T for a single-temperature model or 2T for the Park two-temperature model. Based on this nomenclature, a matrix of sixteen specific test cases is evaluated.

11.2. Stagnation-Point Heat Flux Comparison

Table 11.1 summarises the stagnation-point heat flux q_{stag} obtained for each configuration:

Table 11.1. Stagnation-point heat flux q_{stag} for each configuration (shot 2254).

Case ID	Model description	q_{stag} [W/cm^2]
A-FS-1T	No heat flux, adiabatic, first-order, 1T	N/A
A-SS-1T	No heat flux, adiabatic, second-order, 1T	N/A
A-FS-2T	No heat flux, adiabatic, first-order, 2T	N/A
A-SS-2T	No heat flux, adiabatic, second-order, 2T	N/A
B-FS-1T	Non-catalytic, first-order, 1T	639
B-SS-1T	Non-catalytic, second-order, 1T	617
B-FS-2T	Non-catalytic, first-order, 2T	662
B-SS-2T	Non-catalytic, second-order, 2T	652
C-FS-1T	Supercatalytic, first-order, 1T	718
C-SS-1T	Supercatalytic, second-order, 1T	856
C-FS-2T	Supercatalytic, first-order, 2T	1140
C-SS-2T	Supercatalytic, second-order, 2T	1122
D-FS-1T	Mitcheltree, first-order, 1T	520
D-SS-1T	Mitcheltree, second-order, 1T	739
D-FS-2T	Mitcheltree, first-order, 2T	710
D-SS-2T	Mitcheltree, second-order, 2T	721

11.3. Mesh Adaptation

To obtain credible results in simulations involving shockwaves, the shock region must be accurately resolved. It is essential to capture the shock across multiple cells to ensure numerical stability and physical accuracy. However, uniformly refining the entire computational domain to meet this criterion would be computationally prohibitive. To address this, a mesh adaptation tool is employed, which dynamically divides the grid based on specific, user-defined criteria. While there are numerous parameters available for shock aligned adaptation such as gradients or specific value ranges of density, velocity, or Mach number—the method utilized in this thesis relies on a denity gradient sensor. Starting from an initially unadapted grid, the mesh is iteratively refined in regions exhibiting large $\nabla\rho$. This approach accurately targets the bow shock and strong compression zones, producing the narrow band of highly refined cells necessary for a stable, grid-resolved solution. This approach aligns with the Schlieren imaging technique, widely used in experimental aerodynamics to visualize shockwaves by optically capturing density variations in compressible flows.

11.4. Temperature Contours

To complement the stagnation-point comparison, static temperature contours are generated for each configuration. Table 11.2 lists the figure references for each case.

Table 11.2. Static temperature contour plots for each configuration.

Case ID	Contour figure
A-FS-1T	Fig. 11.1
A-SS-1T	Fig. 11.2
A-FS-2T	Fig. 11.3
A-SS-2T	Fig. 11.4
B-FS-1T	Fig. 11.5
B-SS-1T	Fig. 11.6
B-FS-2T	Fig. 11.7
B-SS-2T	Fig. 11.8
C-FS-1T	Fig. 11.9
C-SS-1T	Fig. 11.10
C-FS-2T	Fig. 11.11
C-SS-2T	Fig. 11.12
D-FS-1T	Fig. 11.13
D-SS-1T	Fig. 11.14
D-FS-2T	Fig. 11.15
D-SS-2T	Fig. 11.16

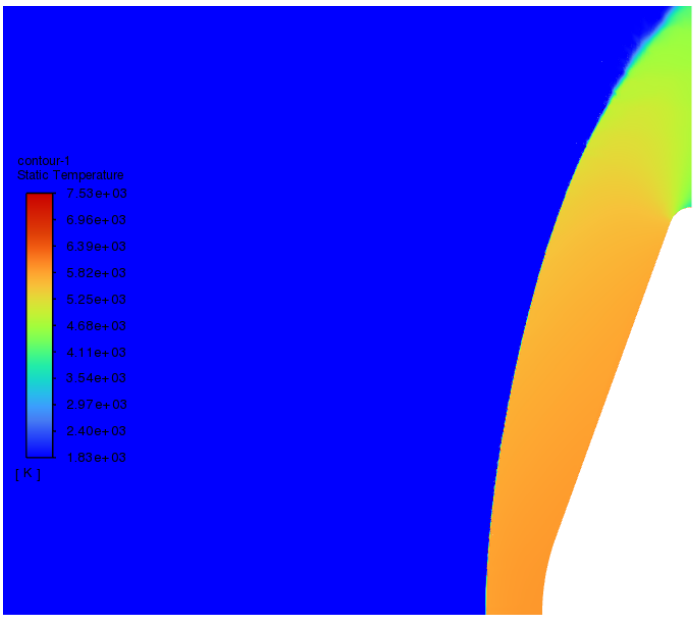


Figure 11.1. Static temperature for A-FS-1T (adiabatic, 1st-order, 1T).

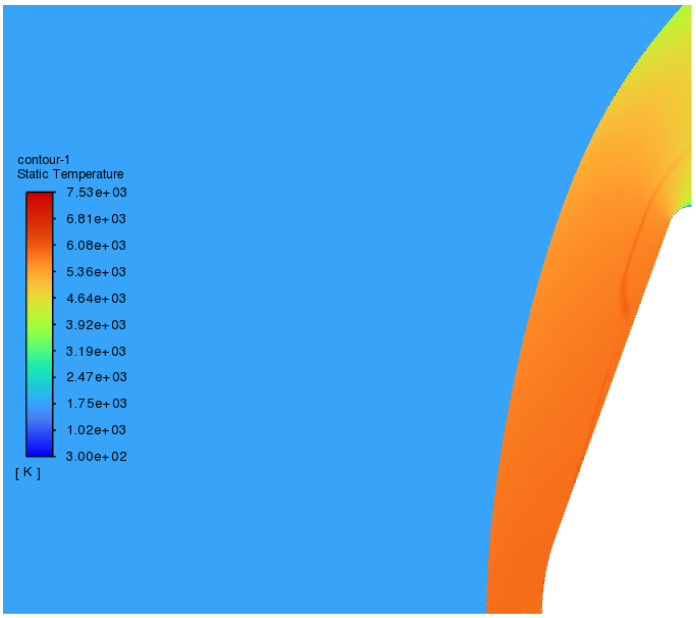


Figure 11.2. Static temperature for A-SS-1T (adiabatic, 2nd-order, 1T).

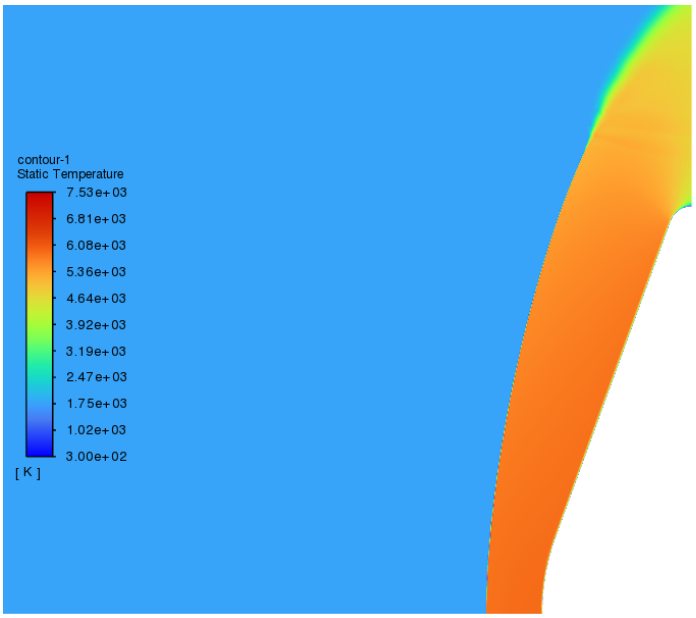


Figure 11.3. Static temperature for A-FS-2T (adiabatic, 1st-order, 2T).

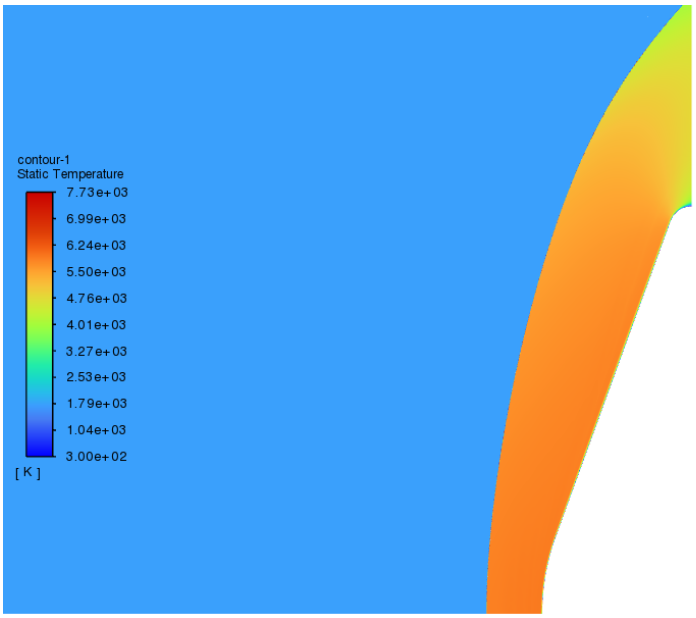


Figure 11.4. Static temperature for A-SS-2T (adiabatic, 2nd-order, 2T).

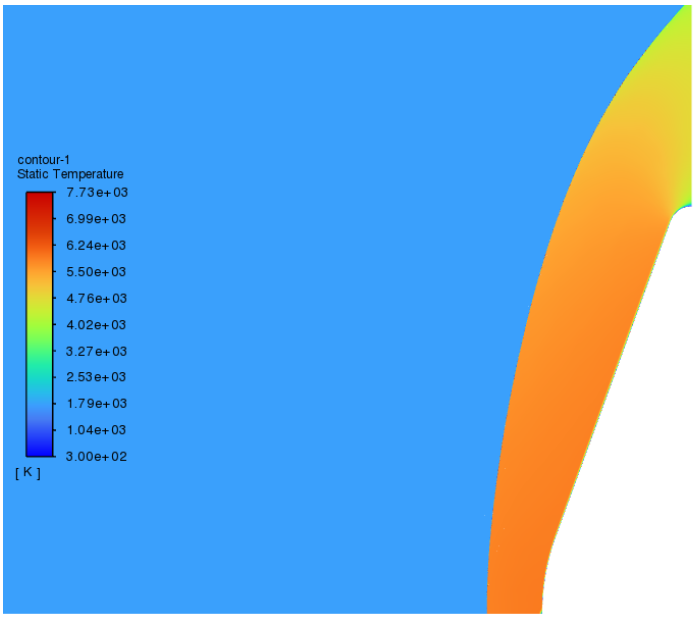


Figure 11.5. Static temperature for B-FS-1T (non-catalytic, 1st-order, 1T).

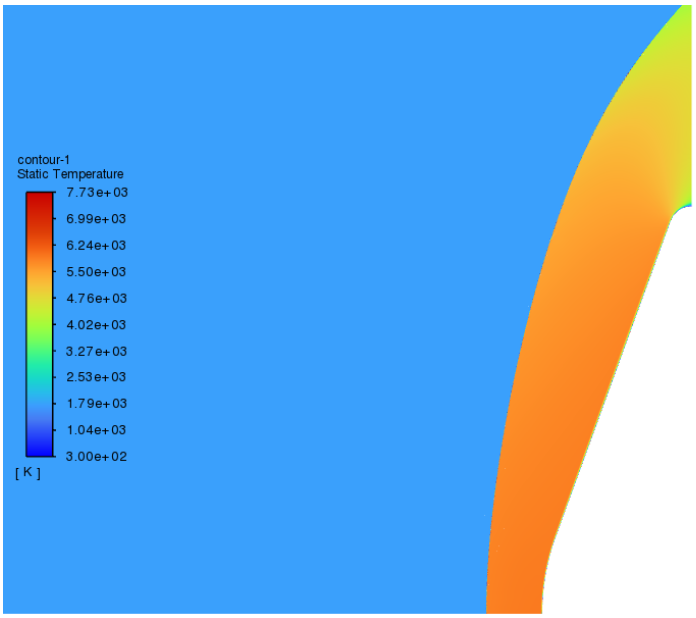


Figure 11.6. Static temperature for B-SS-1T (non-catalytic, 2nd-order, 1T).

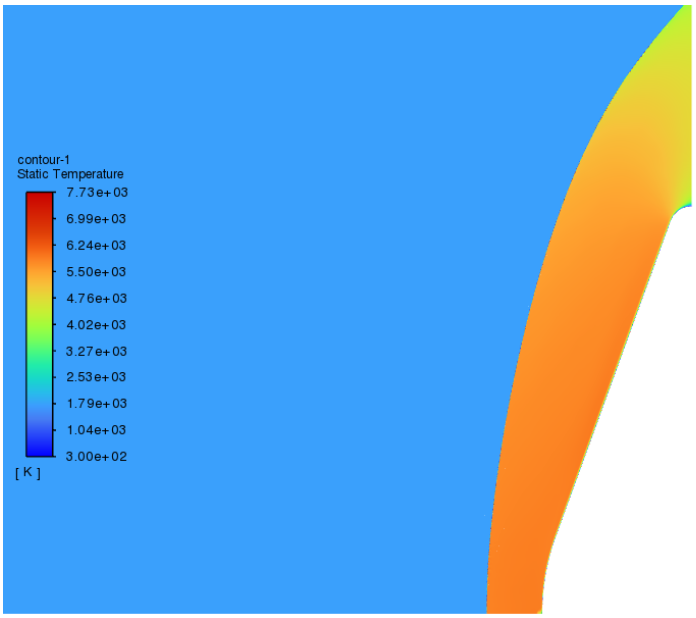


Figure 11.7. Static temperature for B-FS-2T (non-catalytic, 1st-order, 2T).

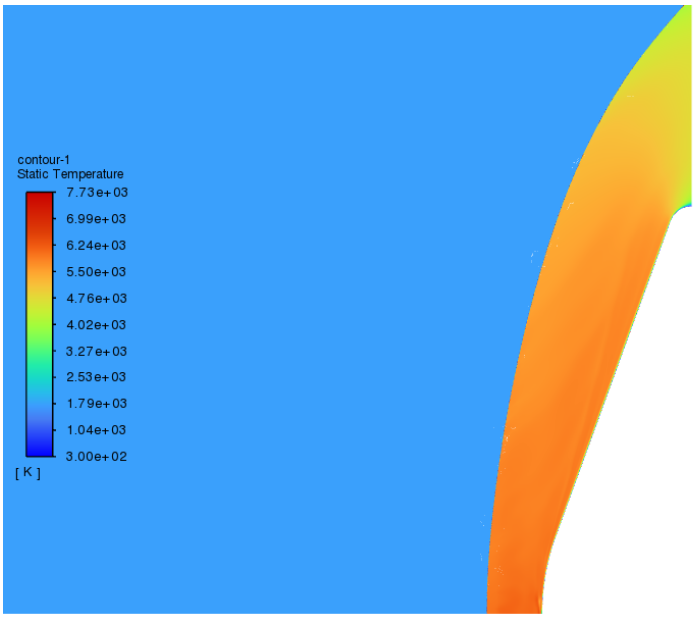


Figure 11.8. Static temperature for B-SS-2T (non-catalytic, 2nd-order, 2T).

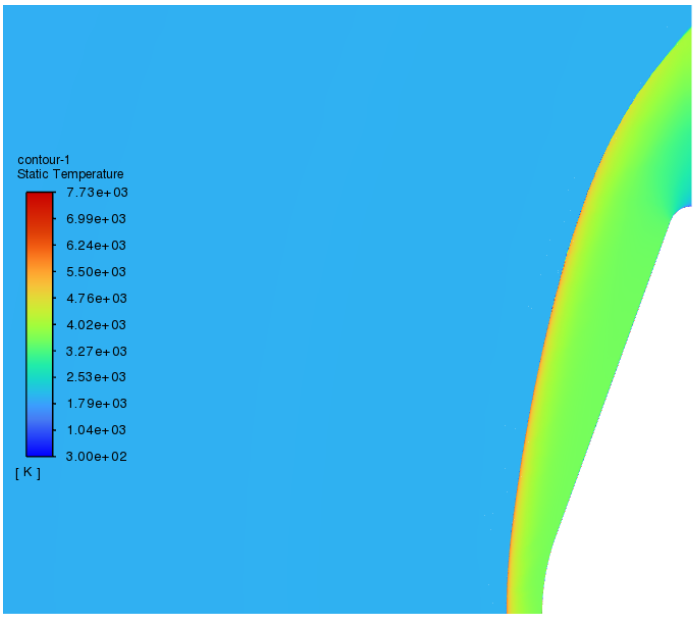


Figure 11.9. Static temperature for C-FS-1T (supercatalytic, 1st-order, 1T).

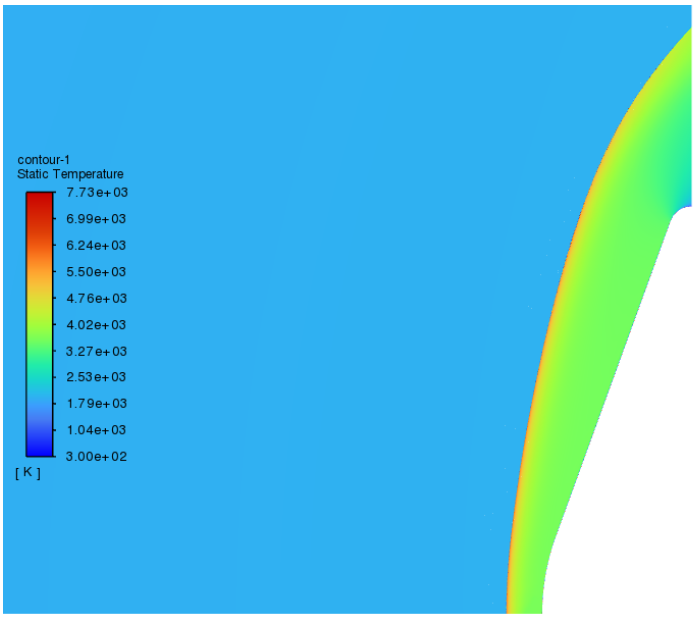


Figure 11.10. Static temperature for C-SS-1T (supercatalytic, 2nd-order, 1T).

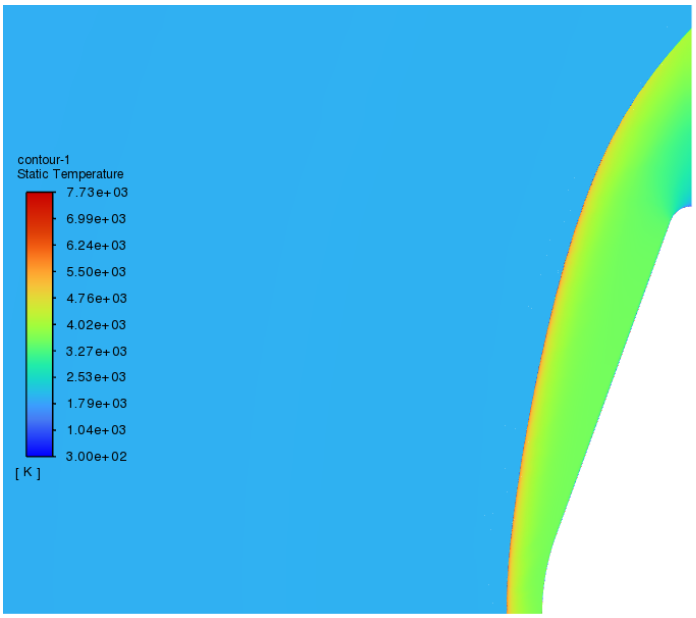


Figure 11.11. Static temperature for C-FS-2T (supercatalytic, 1st-order, 2T).

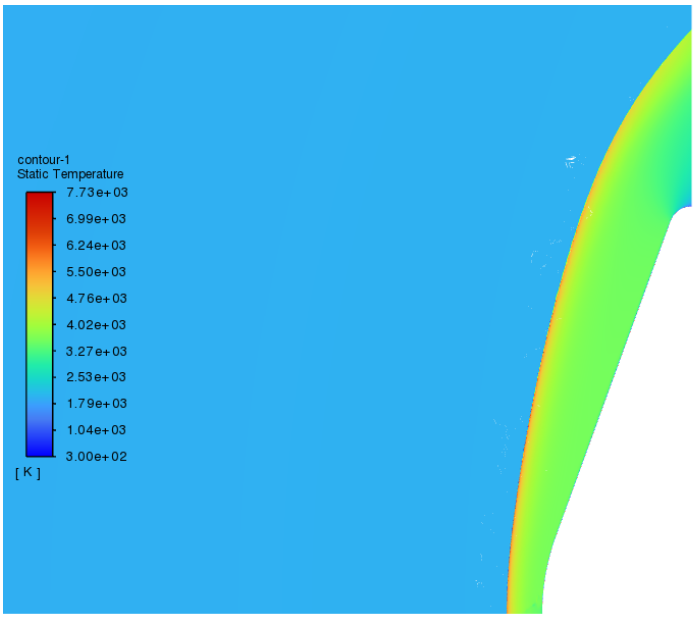


Figure 11.12. Static temperature for C-SS-2T (supercatalytic, 2nd-order, 2T).

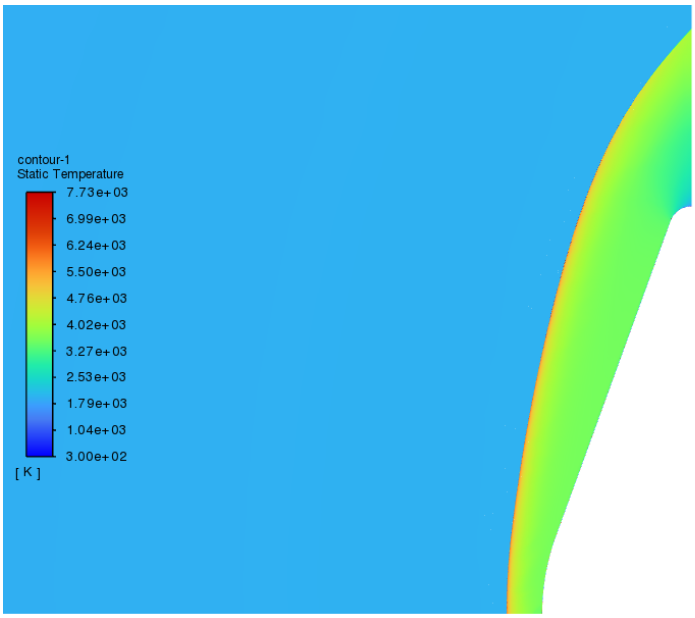


Figure 11.13. Static temperature for D-FS-1T (Mitcheltree, 1st-order, 1T).

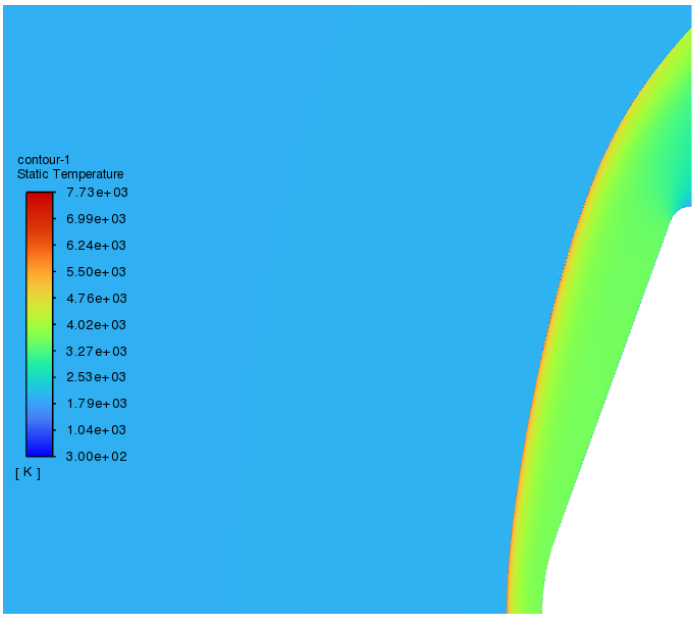


Figure 11.14. Static temperature for D-SS-1T (Mitcheltree, 2nd-order, 1T).

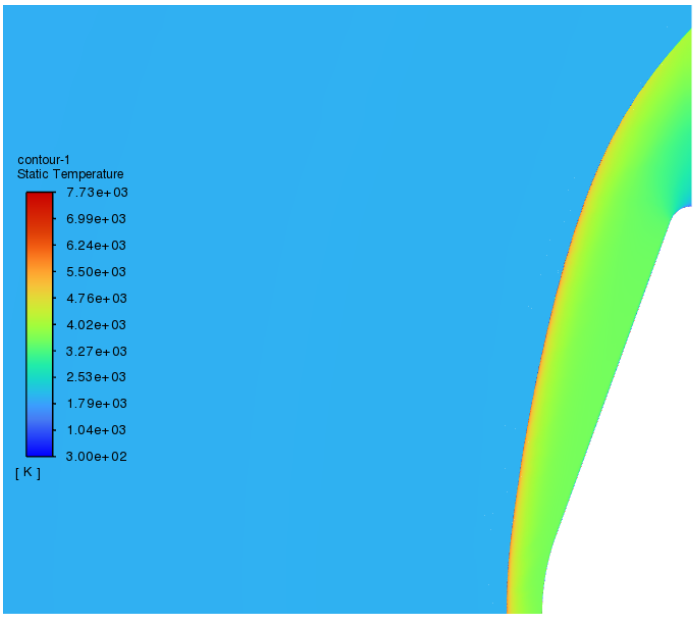


Figure 11.15. Static temperature for D-FS-2T (Mitcheltree, 1st-order, 2T).

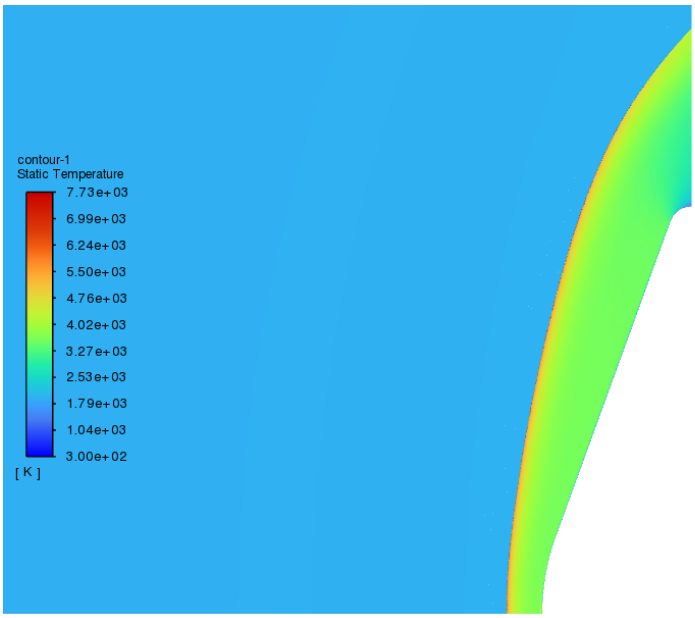


Figure 11.16. Static temperature for D-SS-2T (Mitcheltree, 2nd-order, 2T).

Table 11.3. Comparison of peak shock-layer static temperature T_{shock} and drag coefficient c_d for all CFD configurations at T5 shot 2254 conditions.

Case ID	Wall model	Scheme	Thermal model	T_{shock} [K]
A-FS-1T	Adiabatic	First-order	1T	*6080*
A-SS-1T	Adiabatic	Second-order	1T	*6110*
A-FS-2T	Adiabatic	First-order	2T	*5980*
A-SS-2T	Adiabatic	Second-order	2T	*7730*
B-FS-1T	Non-catalytic	First-order	1T	*5920*
B-SS-1T	Non-catalytic	Second-order	1T	*5940*
B-FS-2T	Non-catalytic	First-order	2T	*7320*
B-SS-2T	Non-catalytic	Second-order	2T	*7290*
C-FS-1T	Supercatalytic	First-order	1T	*6000*
C-SS-1T	Supercatalytic	Second-order	1T	*6060*
C-FS-2T	Supercatalytic	First-order	2T	*7330*
C-SS-2T	Supercatalytic	Second-order	2T	*7400*
D-FS-1T	Mitcheltree	First-order	1T	*5990*
D-SS-1T	Mitcheltree	Second-order	1T	*6200*
D-FS-2T	Mitcheltree	First-order	2T	*7330*
D-SS-2T	Mitcheltree	Second-order	2T	*7530*

Peak temperature of the shockwave 11.3 was plotted, to observe effect of discretization scheme and temperature model on the modeling of the shockwave in the Fluent software. Results obtianed show significant influence of the 2T model on the predicted

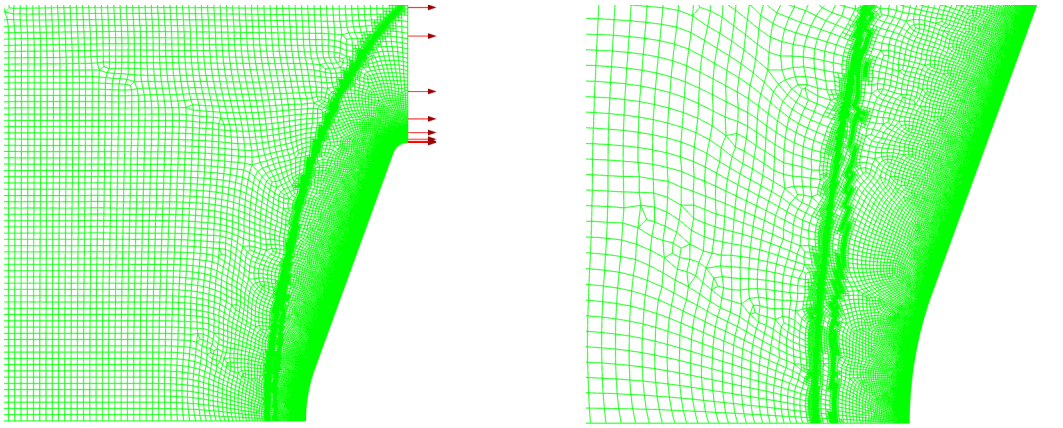
shock temperature, which is expected due to the thermal nonequilibrium between the translational-rotational and vibrational energy modes within the post shock gas mixture. In highly hypersonic flows, the kinetic energy of the freestream is rapidly converted into thermal energy across the bow shock. While the translational-rotational energy modes equilibrate almost immediately upon collision, vibrational excitation is a much slower process that requires a finite relaxation period to absorb this energy. A 1T model assumes instantaneous thermodynamic equilibrium across all internal energy modes, which artificially suppresses the maximum temperature immediately behind the shockwave.

In contrast, the 2T temperature model accounts for this delayed energy transfer by solving separate equations: one for translational-rotational energy of the heavy particles, and a second temperature for slower-to-equilibrate vibrational energy. Because the vibrational modes do not instantaneously absorb their part of the post-shock thermal energy, the translational-rotational temperature retains a larger portion of the total energy, leading to a much higher initial peak. Consequently, the 2T model successfully captures this residual separation between the energy modes in the shock layer, yielding the significantly elevated and more physically accurate static shockwave temperatures observed in the simulations.

11.5. Comparison with Reference Data

The overall trends obtained from the numerical simulations are consistent with expectations and with the reference data from the T5 shock-tunnel campaign on the MSL aeroshell [1]. In all cases, second-order solutions reproduce both the magnitude and qualitative distribution of the surface heat flux reported in the article, whereas first-order solutions exhibit significant numerical dissipation, leading to inexact shockwaves position and distorted heating profiles. Moreover 2T model tends to provide better and more accurate results than 1T model.

All solutions employ mentioned previously in the thesis shock-aligned mesh refinement based on a density-gradient sensor. Starting from an initially unadapted grid, the mesh is iteratively refined in regions of large $\nabla\rho$, corresponding to the bow shock and strong compression zones. This produces a narrow band of highly refined cells aligned with the shock, as illustrated in Fig. 11.17, and is essential for obtaining stable, grid-resolved solutions.



(a) Overview of adapted meshes (FS and SS)

(b) Closeup of adapted meshes (FSand SS)

Figure 11.17. Adapted meshes of B-SS-1T and B-FS-1T case

The visual comparison of the adapted meshes for the B-FS-1T and B-SS-1T cases reveals a distinct difference in the resulting shock stand-off distance. Because the mesh adaptation algorithm inherently tracks the pressure gradient, the highly refined band of cells traces the numerical shock location. In the first-order solution (B-FS-1T), the shock is displaced farther from the body. Conversely, the second-order scheme (B-SS-1T) yields a sharper, drawing the adapted mesh band closer to the forebody and reducing the overall shock stand-off distance.

11.5.1. Non-Catalytic Wall

For the non-catalytic wall, the absence of recombination at the surface leads to the lowest heating levels among the three wall models. Second-order non-catalytic solutions yield stagnation-point heat fluxes that are systematically below the experimental values, reproducing the trend reported by Wright [1].

11.5.2. Supercatalytic Wall

For the supercatalytic wall, all incident dissociated species recombine to CO_2 at the surface, maximising recovery of chemical enthalpy. In this configuration, second-order solutions (C-SS-1T / C-SS-2T) provide the best overall agreement with the T5 data, closely matching the DPLR/LAURA results reported in the article.

11.5.3. Mitcheltree Catalytic Wall

The Mitcheltree wall model represents an intermediate level of catalysis, with recombination controlled by surface reaction rates. Mitcheltree cases produce stagnation-point heating levels between the non-catalytic and supercatalytic limits. This confirms that correct representation of wall chemistry is the primary requirement for matching the T5 data.

11.5.4. Obtained Data

Figures 11.18 and 11.19 compare the centerline aeroheating peaks obtained with the single-temperature and two-temperature first-order schemes for the three wall catalysis models (non-catalytic, Mitcheltree, supercatalytic) at the T5 2254 conditions. In the 1T FS case, the stagnation-point heat flux reaches approximately $q_{\text{stag}} \approx 720$ W/cm^2 for the supercatalytic wall, 640 W/cm^2 for the non-catalytic wall, and 520 W/cm^2 for the Mitcheltree model, with relatively rounded centerline peaks and modest shoulder maxima. Although the non-catalytic CFD curve agrees reasonably well with the corresponding Wright et al. reference, both the supercatalytic and Mitcheltree solutions underpredict the experimentally inferred stagnation heating levels.

Introducing the two-temperature model while retaining the first-order spatial scheme (2T-FS, Fig. 11.19) substantially modifies both the magnitude and the separation of the catalytic limits. The supercatalytic stagnation value increases to about $q_{\text{stag}} \approx 1140$ W/cm^2, bringing the CFD prediction into close agreement with the laminar supercatalytic reference from Wright [1], whereas the Mitcheltree and non-catalytic peaks rise to roughly 710 W/cm^2 and 660 W/cm^2, respectively. The central peak becomes noticeably steeper, and the spread between catalytic models is amplified: the supercatalytic wall clearly defines an upper bound, the non-catalytic case remains the lower bound, and the Mitcheltree result shifts upward toward the supercatalytic curve, consistent with its fully catalytic but diffusion-limited character.

Along the shoulders, the 2T-FS solutions also show slightly higher heating levels and more pronounced local peaks than the 1T-FS counterparts, particularly for the catalytic walls. These differences reflect the additional vibrational nonequilibrium energy captured by the two-temperature formulation, which increases the available post-shock enthalpy and strengthens the sensitivity of surface heat flux to wall catalysis. Overall, even in combination with a dissipative first-order scheme, the two-temperature model is required to reproduce the experimentally observed separation between catalytic and non-catalytic heating levels at the stagnation point and along the forebody.

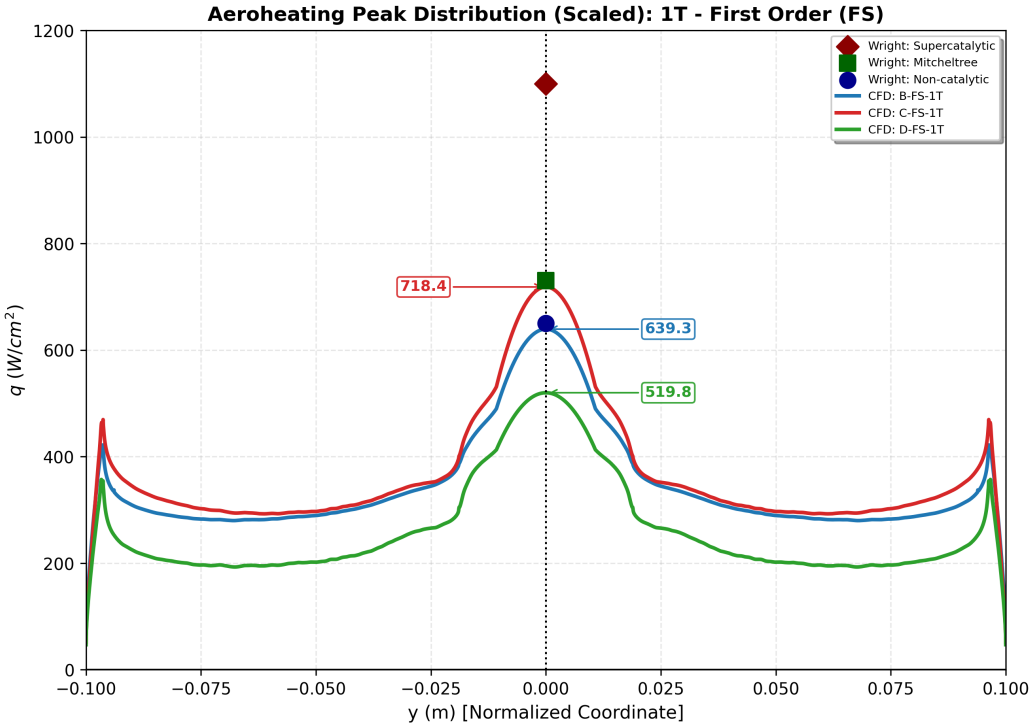


Figure 11.18. Aeroheating peak distribution for the 1T-FS simulations with non-catalytic, supercatalytic, and Mitcheltree wall models, compared against the corresponding Wright et al. reference values.

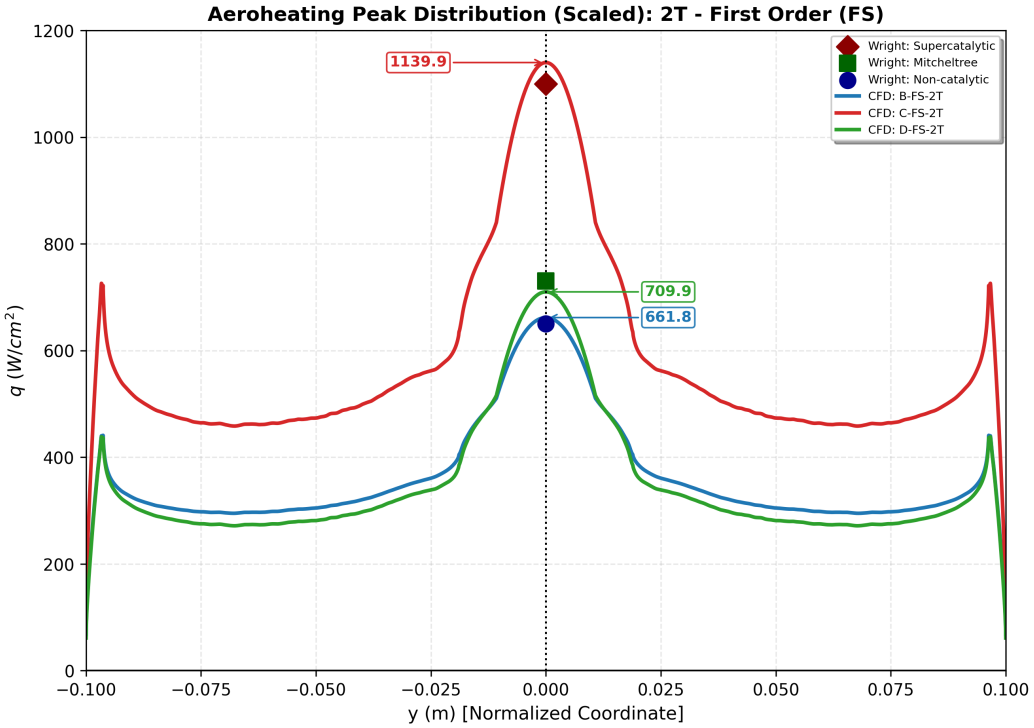


Figure 11.19. Aeroheating peak distribution for the 2T-FS simulations with non-catalytic, supercatalytic, and Mitcheltree wall models, compared against the corresponding Wright et al. reference values.

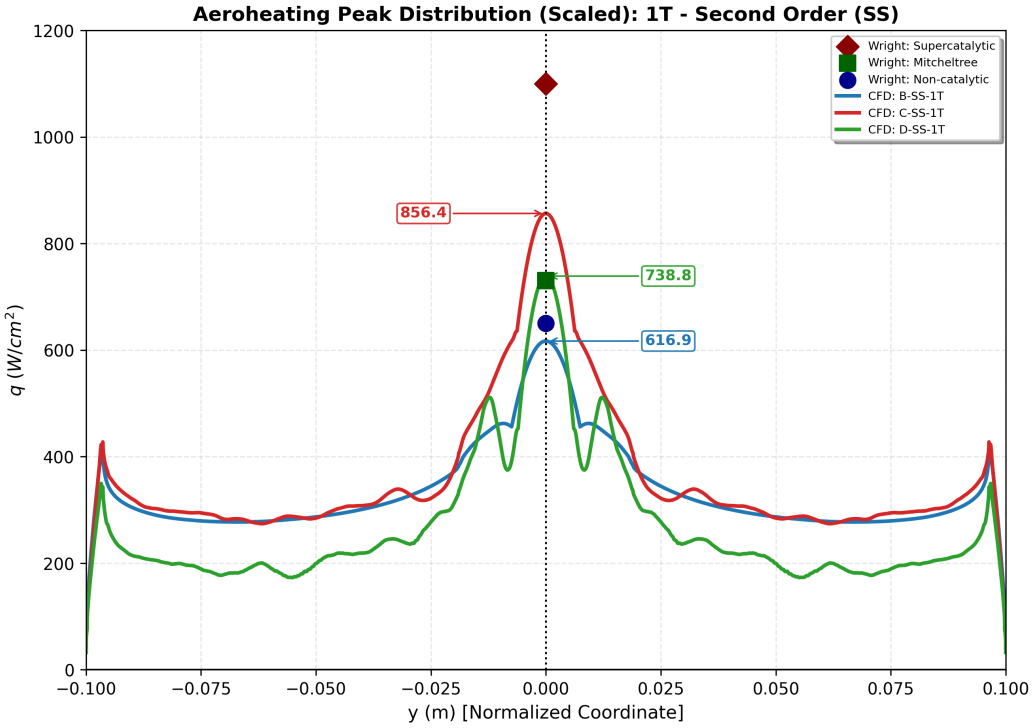


Figure 11.20. Aeroheating peak distribution for the 1T-SS simulations with non-catalytic, supercatalytic, and Mitcheltree wall models, compared against the corresponding Wright et al. reference values.

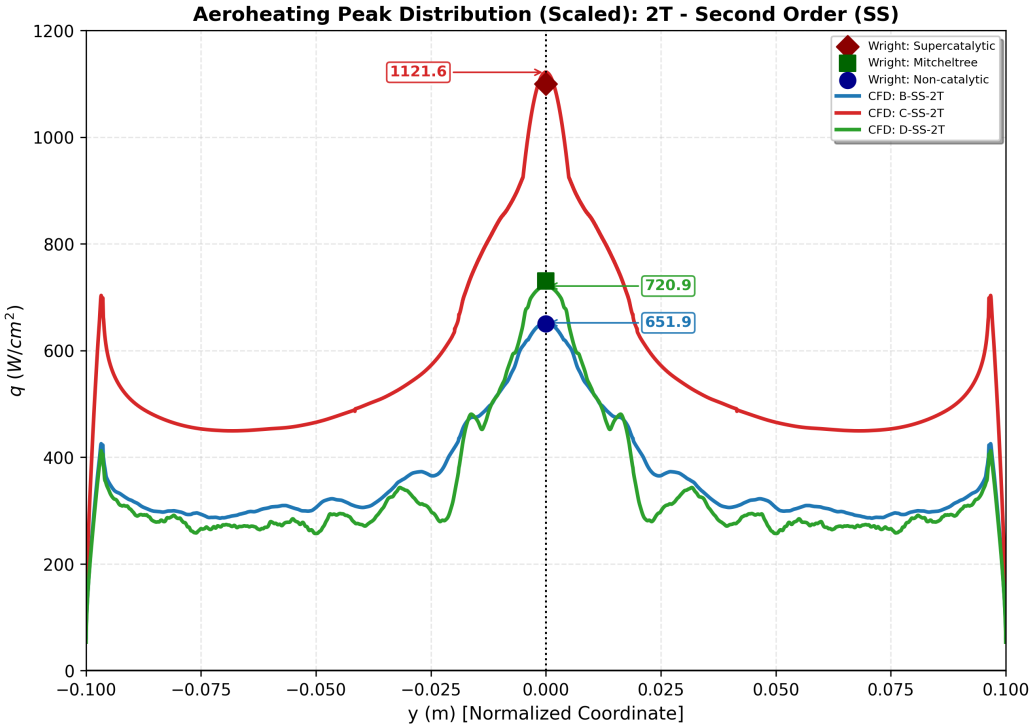


Figure 11.21. Aeroheating peak distribution for the 2T-SS simulations with non-catalytic, supercatalytic, and Mitcheltree wall models, compared against the corresponding Wright et al. reference values.

As can be seen, the 2T-FS configurations provide the closest agreement with the reference article data, both in terms of peak magnitude and overall shape of the heating distribution. For this reason, these computational settings are selected as the most reliable baseline for the subsequent comparison with the results reported in the figure (11.23).

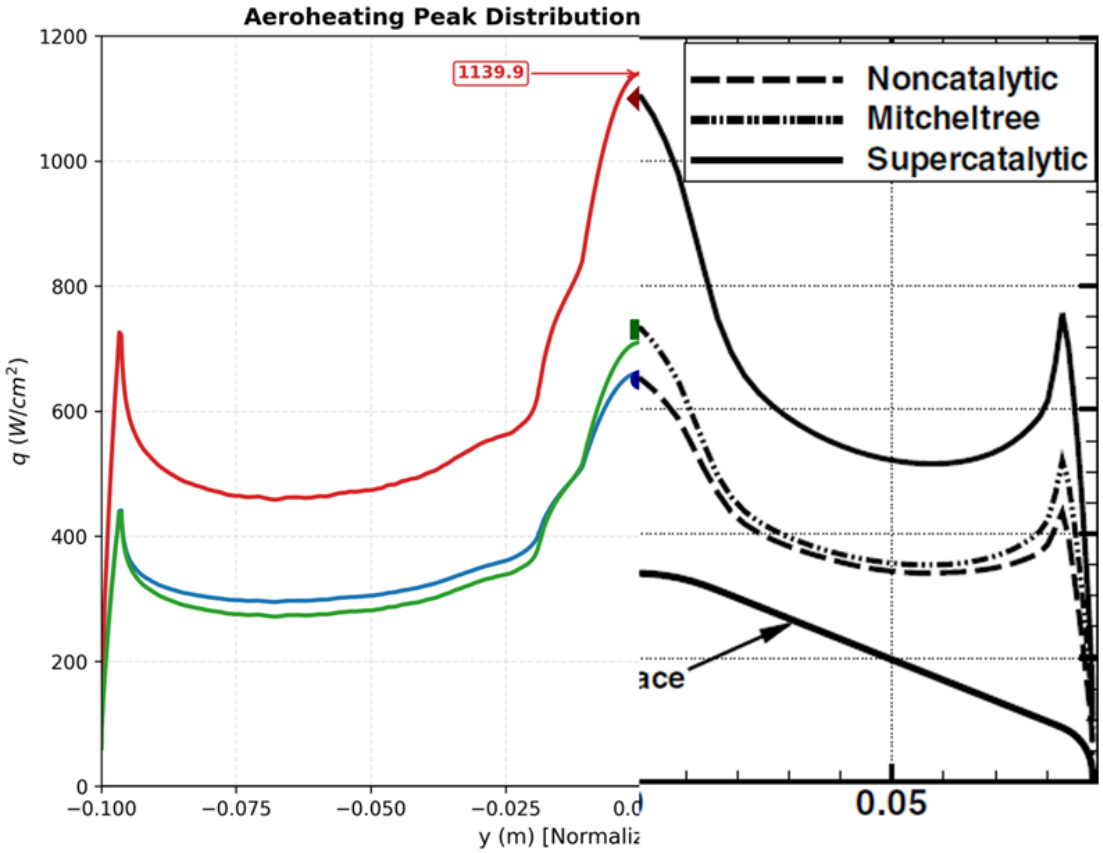


Figure 11.22. 2T-FS case comparison with article [1] data

The 2T-FS simulation demonstrates a reasonable correlation with the reference data provided by Wright [1]. Despite utilizing first-order spatial discretization schemes, the resulting heat flux profile captures the fundamental aerodynamic heating trends with acceptable accuracy.

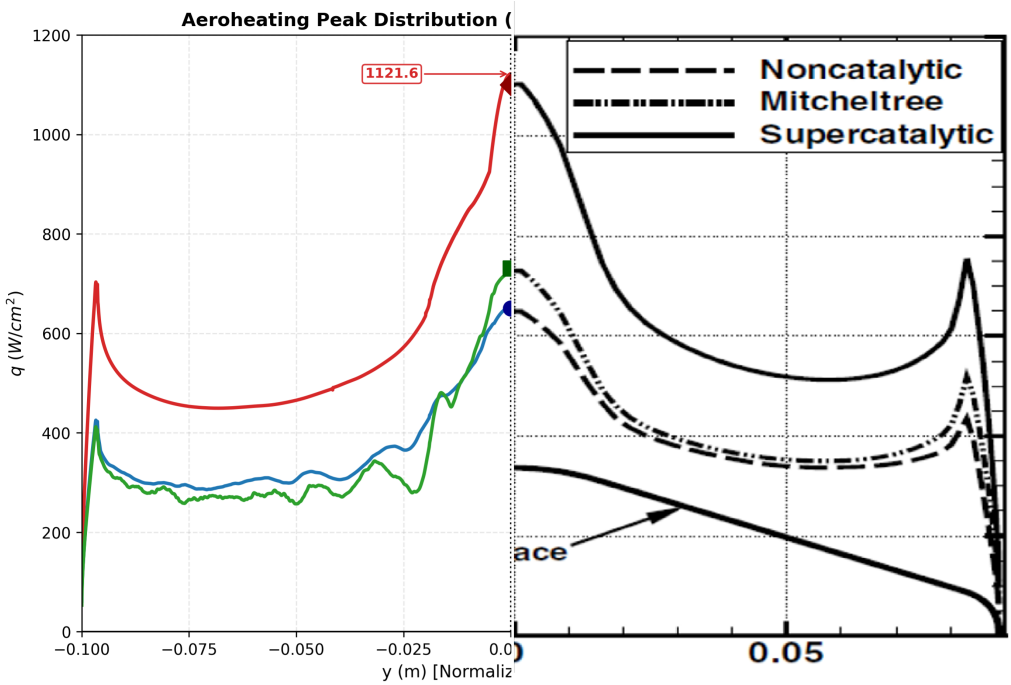


Figure 11.23. 2T-SS case comparison with article [1] data

The heat-flux distribution predicted with the 2T-SS settings shows the best overall agreement with the reference article, both at the stagnation point and near the secondary peaks toward the ends of the profile. In particular, the model captures not only the main maximum but also the rise in heating toward the shoulder regions with the correct magnitude and general trend, indicating that the selected thermal and numerical assumptions reproduce the full forebody heating pattern consistently. This Fluent analysis is also in good agreement with the DPLR results reported in the article, which further supports the validity of the chosen setup and gives confidence that these CFD settings provide the most reliable basis for the comparison with the published data 11.23. Only disadvantage of the 2T-SS approach compared to 2T-FS is the oscilation of results of Mitcheltree solution.

12. Summary

As stated in the Motivation 2.2 section, the goal was to validate the Ansys Fluent software with the Wright [1] experimental and CFD data. Numerous different models were applied to check their influence on the obtained in the Wright's [1] results. Settings consisted of two different temperature models, particularly 1 temperature and 2 temperature model. Wall Catalysis models were another variable factor in the analyses, as non-catalytic, Mitcheltree, and fully catalytic wall models. Moreover first and second order discretization schemes were taken into account.

Data obtained in the work provide valuable information on influence of mentioned above parameters on physics of the solution. The primary quantity that was observed and compared with Wright's [1] work was heat flux. Although first and second order solution with 1T settings cases converged and their results are trustworthy (11.18, 11.20), the peak heat flux at the stagnation point was much lower then expected in the Wright's [1] article. Overall behaviour and heat flux distribution was correct with two peaks at the sides of the aeroshell and one at the stagnation point.

On the other hand, both first and second order solutions used with 2T temperature model 11.19, 11.21) tend to predict the peak heat flux at the stagnation point and the peaks on sides of the aeroshell pretty accurately. Although the numerical value of these two peaks is insignificantly different, the behaviour of Mitcheltree and noncatalytic model for second order solution is oscilatory. Due to this, one can admit that temperature model is of much greater influence on the solution than the order of the discretization scheme.

13. Acknowledgements

I would first like to express my deepest gratitude to my supervisor, **Dr. Michał Remer**, for his constant support, guidance, and patience throughout this thesis. His willingness to devote time to discussions, carefully read drafts, and provide detailed feedback has been invaluable for the development of both this work and my own scientific thinking.

I am especially grateful for his openness to new ideas and for encouraging me to explore my own concepts, even the unconventional ones. His ability to challenge my assumptions while still giving me the freedom to make independent decisions has been crucial in shaping this project. The many conversations about hypersonic flows, aerothermodynamics, and numerical modeling not only helped to clarify technical issues, but also inspired several of the directions pursued in this thesis.

References

[1] M. J. Wright, J. Olejniczak, J. L. Brown, H. G. Hornung, and K. T. Edquist, "Modeling of shock tunnel aeroheating data on the mars science laboratory aeroshell", *Journal of Thermophysics and Heat Transfer*, vol. 20, no. 4, pp. 641–651, 2006. DOI: 10.2514/1.19896. [Online]. Available: https://doi.org/10.2514/1.19896.

[2] J. Urzay, "The physical characteristics of hypersonic flows", Center for Turbulence Research, Stanford University, Stanford, CA 94305, Tech. Rep., Jul. 2020, Technical report.

[3] W. E. Meador, G. A. Miner, and J. H. Heinbockel, "Vibrational relaxation in hypersonic flow fields", NASA Langley Research Center, Hampton, VA, NASA Technical Paper 3367, Sep. 1993.

[4] J. D. A. Jr., *Hypersonic and High Temperature Gas Dynamics*, 2nd. Reston, Virginia: AIAA Education Series, American Institute of Aeronautics and Astronautics, 2006, ISBN: 978-1-56347-892-3.

[5] Wikipedia contributors. "Law of the wall". [Online; accessed March 2, 2025]. (n.d.), [Online]. Available: https://en.wikipedia.org/wiki/Law_of_the_wall.

[6] Wikipedia contributors, *Knudsen number — Wikipedia, the free encyclopedia*, Accessed: 2025-05-21, 2024. [Online]. Available: https://en.wikipedia.org/wiki/Knudsen_number.

[7] P. A. Gnoffo, R. N. Gupta, and J. L. Shinn, "Conservation equations and physical models for hypersonic air flows in thermal and chemical nonequilibrium", NASA, Washington, DC, NASA Technical Paper NASA TP-2867, Feb. 1989.

[8] C. Kim, K. H. Kim, Y. Yang, and J. G. Kim, "Effect of multi-temperature models on heat transfer and electron behavior in hypersonic flows", *Physics of Fluids*, vol. 36, no. 9, p. 096 127, 2024. DOI: 10.1063/5.0223900.

[9] N. /. J. P. Laboratory *et al.*, *Aerothermodynamics course, short course materials from thermal & fluids analysis workshop (tfaws 2012)*, https://tfaws.nasa.gov/TFAWS12/Proceedings/Aerothermodynamics%20Course.pdf, [Online; accessed: 2025-05-26], 2012.

[10] Y. Prévereaud, J.-L. Vérant, and J. Annaloro, "Noncatalytic and finite catalytic heating models for atmospheric re-entry codes", in *Proceedings of the First International Orbital Debris Conference (Orbital Debris 2019)*, [Online; accessed: 2025-05-26], Houston, USA, 2019, p. 6112. [Online]. Available: https://www.hou.usra.edu/meetings/orbitaldebris2019/orbital2019paper/pdf/6112.pdf.

[11] T. K. West IV and A. M. Brandis, "Updated stagnation point aeroheating correlations for mars entry", in *12th Joint AIAA/ASME Thermophysics and Heat Transfer Conference*, [Online; accessed: 2025-09-14], Atlanta, GA, USA: American Institute of Aeronautics and Astronautics, 2018, pp. 520–532. DOI: 10.2514/6.2018-3767. [Online]. Available: https://arc.aiaa.org/doi/10.2514/6.2018-3767.

[12] V. Carandente, R. Savino, M. Iacovazzo, and C. Boffa, "Aerothermal analysis of a sample-return reentry capsule", in *Proceedings of the 5th European Conference for Aeronautics and Space Sciences (EUCASS 2013)*, [Online; accessed: 2025-05-26], Munich, Germany, 2013. [Online]. Available: https://www.eucass.eu/doi/EUCASS2013-448.pdf.

[13] J. Urzay, "The physical characteristics of hypersonic flows", *Center for Turbulence Research, Stanford University*, Jul. 2020, [Online; accessed: 2025-05-26]. [Online]. Available: https://web.stanford.edu/~jurzay/Urzay_Hypersonics_2020.pdf.

[14] B. A. Cruden and A. M. Brandis, "Investigation of non-equilibrium radiation for earth entry", in *11th AIAA/ASME Joint Thermophysics and Heat Transfer Conference*, ser. AIAA Paper 2016-3243, [Online; accessed: 2025-05-26], Washington, D.C., 2016. DOI: 10.2514/6.2016-3243. [Online]. Available: https://ntrs.nasa.gov/citations/20160009760.

[15] Y. Zhang, "A review of advances in thermal protection systems and insulation materials for hypersonic vehicles", *Journal of Physics: Conference Series*, vol. 2026, no. 1, p. 012 027, 2021, [Online; accessed: 2025-05-26]. DOI: 10.1088/1742-6596/2026/1/012027. [Online]. Available: https://iopscience.iop.org/article/10.1088/1742-6596/2026/1/012027.

[16] D. E. Glass, "Ceramic matrix composite (cmc) thermal protection systems (tps) and hot structures for hypersonic vehicles", in *15th AIAA International Space Planes and Hypersonic Systems and Technologies Conference*, [Online; accessed: 2025-05-26], Orlando, FL, USA, Apr. 2008. DOI: 10.2514/6.2008-2583. [Online]. Available: https://ntrs.nasa.gov/citations/20080017004.

[17] M. Mahzari and T. White, "Mars science laboratory heatshield flight data and analysis", in *Hypersonic Vehicle Flight Prediction Workshop*, [Online; accessed: 2025-05-26], NASA Ames Research Center, Moffett Field, CA, USA, Jun. 2017. [Online]. Available: https://ntrs.nasa.gov/citations/20170005728.

[18] CFD Online, *Introduction to turbulence/reynolds averaged equations – turbulence closure problem and eddy viscosity*, https://www.cfd-online.com/Wiki/Introduction_to_turbulence/Reynolds_averaged_equations#Turbulence_closure_problem_and_eddy_viscosity, Accessed: 2025-05-26, n.d.

[19] CFD Online, *Boussinesq eddy viscosity assumption*, https://www.cfd-online.com/Wiki/Boussinesq_eddy_viscosity_assumption, Accessed: 2025-05-26, n.d.

[20] CFD Online, *Favre averaged navier-stokes equations*, https://www.cfd-online.com/Wiki/Favre_averaged_Navier-Stokes_equations, Accessed: 2025-05-26, n.d.

[21] CFD Online, *Sst k-omega model*, https://www.cfd-online.com/Wiki/SST_k-omega_model, Accessed: 2025-05-26, n.d.

[22] *Ansys fluent user's guide: Section 7.3.9 – pressure far-field boundary conditions*, Pressure far-field characteristic boundary condition; limitations and applicability, ANSYS Inc., 2006. [Online]. Available: https://www.afs.enea.it/project/neptunius/docs/fluent/html/ug/node245.htm.

[23] ANSYS Inc. "Symmetry boundary conditions — ansys fluent user's guide (section 7.3.15)". Accessed: 2025-??-?? (2009).

[24] S. Yu, X. Ni, and F. Chen, "Cfd simulation strategy for hypersonic aerodynamic heating around a blunt biconic", *International Journal of Aerospace Engineering*, vol. 2021, pp. 1–11, 2021. DOI: 10.1155/2021/8885074. [Online]. Available: https://doi.org/10.1155/2021/8885074.

[25] X. Liang, X. Li, D. Fu, and Y. Ma, "Dns of a spatially evolving hypersonic turbulent boundary layer at mach 8", *Science China Physics, Mechanics & Astronomy*, vol. 56, no. 7, pp. 1408–1418, 2013. DOI: 10.1007/s11433-013-5102-9. [Online]. Available: https://doi.org/10.1007/s11433-013-5102-9.

[26] A. Patel, J. W. R. Peeters, B. J. Boersma, and R. Pecnik, "Semi-local scaling and turbulence modulation in variable property turbulent channel flows", *Physics of Fluids*, vol. 27, no. 9, p. 095 101, 2015. DOI: 10.1063/1.4929813. [Online]. Available: https://doi.org/10.1063/1.4929813.

[27] D. Bose, J. L. Brown, D. K. Prabhu, P. Gnoffo, C. O. Johnston, and B. Hollis, "Uncertainty assessment of hypersonic aerothermodynamics prediction capability", NASA Ames Research Center and NASA Langley Research Center, Moffett Field, CA, USA; Hampton, VA, USA, Tech. Rep., n.d. Technical report.

[28] NASA Glenn Research Center. "Wind tunnel test errors tutorial". [Online; accessed March 2, 2025]. (n.d.).

[29] C. S. Analysis. "Determining mesh quality and accuracy parameters". [Online; accessed March 2, 2025]. (2022).

[30] CFD-Online Forums. "Skewness in cfd - discussion thread". [Online; accessed March 2, 2025]. (n.d.), [Online]. Available: https://www.cfd-online.com/Forums/fluent/36272-skewness.html.

[31] C. Williams, M. Di Renzo, and J. Urzay, "Two-temperature extension of the HTR solver for hypersonic turbulent flows in thermochemical nonequilibrium", *Center for Turbulence Research Annual Research Briefs*, pp. 345–358, 2021, [Online; accessed: 2025-05-26]. [Online]. Available: https://ctr.stanford.edu/sites/g/files/sbiybj24451/files/media/file/brief01_2.pdf.

[32] C. Garbacz, F. Morgado, and M. Fossati, "Effect of thermal nonequilibrium on the shock interaction mechanism for carbon dioxide mixtures on double-wedge geometries", *Physics of Fluids*, vol. 34, no. 2, p. 026 108, 2022, [Online; accessed: 2025-05-26]. DOI: 10.1063/5.0078233. [Online]. Available: https://aip.scitation.org/doi/10.1063/5.0078233.

List of Figures

1.1 MSL tested geometry [1] . . . 12
2.1 Laminar centerline heat-transfer distributions for T5 shot 2254 from Wright [1], comparing non-catalytic, Mitcheltree, and supercatalytic wall models. This profile serves as the primary experimental reference for the present CFD study. . . . 15
2.2 Computed mole fractions of CO_2, CO, O_2, and O along the stagnation streamline for shot 2254, comparing non-catalytic, Mitcheltree, and supercatalytic wall models (adapted from Wright[1]). . . . 16
5.1 Geometry of the 70° sphere-cone model: (a) metal test article with thermocouple ports, (b) corresponding 2D profile used in the present analysis. 29
6.1 Illustrative flight trajectories of selected hypersonic vehicles and the approximate onset of vibrational excitation [13] . . . 32
6.2 SPS CMC TPS array for thermal-mechanical testing [16] . . . 33
6.3 Standard PICA model [16] . . . 34
6.4 One of derivatives of PICA [16] . . . 34
6.5 active TPS way of work [15] . . . 35
7.1 Boundary Layer subdivisions [5] . . . 44
8.1 Mesh sensitivity study showing overall grid domain and boundary layer close-ups (Part 1). . . . 47
8.1 Mesh sensitivity study showing overall grid domain and boundary layer close-ups (Part 2). . . . 48
9.1 Freestream 2254 shot conditions . . . 53
10.1 Computational domain used in the simulations. . . . 55
11.1 Static temperature for A-FS-1T (adiabatic, 1st-order, 1T). . . . 58
11.2 Static temperature for A-SS-1T (adiabatic, 2nd-order, 1T). . . . 59
11.3 Static temperature for A-FS-2T (adiabatic, 1st-order, 2T). . . . 59
11.4 Static temperature for A-SS-2T (adiabatic, 2nd-order, 2T). . . . 60
11.5 Static temperature for B-FS-1T (non-catalytic, 1st-order, 1T). . . . 60
11.6 Static temperature for B-SS-1T (non-catalytic, 2nd-order, 1T). . . . 61
11.7 Static temperature for B-FS-2T (non-catalytic, 1st-order, 2T). . . . 61
11.8 Static temperature for B-SS-2T (non-catalytic, 2nd-order, 2T). . . . 62
11.9 Static temperature for C-FS-1T (supercatalytic, 1st-order, 1T). . . . 62
11.10 Static temperature for C-SS-1T (supercatalytic, 2nd-order, 1T). . . . 63
11.11 Static temperature for C-FS-2T (supercatalytic, 1st-order, 2T). . . . 63
11.12 Static temperature for C-SS-2T (supercatalytic, 2nd-order, 2T). . . . 64
11.13 Static temperature for D-FS-1T (Mitcheltree, 1st-order, 1T). . . . 64
11.14 Static temperature for D-SS-1T (Mitcheltree, 2nd-order, 1T). . . . 65
11.15 Static temperature for D-FS-2T (Mitcheltree, 1st-order, 2T). . . . 65

11.16 Static temperature for D-SS-2T (Mitcheltree, 2nd-order, 2T). 66
11.17 Adapted meshes of B-SS-1T and B-FS-1T case 68
11.18 Aeroheating peak distribution for the 1T-FS simulations with non-catalytic, supercatalytic, and Mitcheltree wall models, compared against the corresponding Wright et al. reference values. 70
11.19 Aeroheating peak distribution for the 2T-FS simulations with non-catalytic, supercatalytic, and Mitcheltree wall models, compared against the corresponding Wright et al. reference values. 70
11.20 Aeroheating peak distribution for the 1T-SS simulations with non-catalytic, supercatalytic, and Mitcheltree wall models, compared against the corresponding Wright et al. reference values. 71
11.21 Aeroheating peak distribution for the 2T-SS simulations with non-catalytic, supercatalytic, and Mitcheltree wall models, compared against the corresponding Wright et al. reference values. 71
11.22 2T-FS case comparison with article [1] data 72
11.23 2T-SS case comparison with article [1] data 73

List of Tables

4.1 Shot 2254 laminar stagnation point heat flux estimates for different models and assumptions. 27
8.1 Mesh Sensitivity Study Data 47
8.2 Mesh Sensitivity Simulation Settings 48
11.1 Stagnation-point heat flux q_{stag} for each configuration (shot 2254). 57
11.2 Static temperature contour plots for each configuration. 58
11.3 Comparison of peak shock-layer static temperature T_{shock} and drag coefficient c_d for all CFD configurations at T5 shot 2254 conditions. 66
A.1 NASA-9 polynomial coefficients for CO_2. 81
A.2 NASA-9 polynomial coefficients for O. 81
A.3 NASA-9 polynomial coefficients for C. 81
A.4 NASA-9 polynomial coefficients for O_2. 82
A.5 NASA-9 polynomial coefficients for CO. 82

List of Appendices

1. Nasa 9 coefficients 81

Appendix 1. Nasa 9 coefficients

Table A.1. NASA-9 polynomial coefficients for CO_2.

Coefficient	200–1000 K	1000–6000 K	6000–20000 K
a_1	9.340018×10^{6}	2.223584×10^{7}	-2.917762×10^{11}
a_2	-1.183478×10^{5}	-3.379484×10^{5}	1.921053×10^{8}
a_3	1.001642×10^{3}	1.566476×10^{3}	-4.839069×10^{4}
a_4	4.729915×10^{-1}	-1.742787×10^{-2}	6.365554
a_5	-4.014079×10^{-5}	9.199934×10^{-7}	-4.120742×10^{-4}
a_6	-1.45311×10^{-7}	$-3.574572 \times 10^{-10}$	1.320833×10^{-8}
a_7	5.38431×10^{-11}	1.19602×10^{-13}	-1.67051×10^{-13}

Table A.2. NASA-9 polynomial coefficients for O.

Coefficient	200–1000 K	1000–6000 K	6000–20000 K
a_1	-4.133285×10^{6}	1.361037×10^{8}	9.245023×10^{10}
a_2	8.352085×10^{4}	-3.792956×10^{5}	-5.624579×10^{7}
a_3	1.021797×10^{3}	1.723851×10^{3}	1.460688×10^{4}
a_4	5.267781×10^{-1}	-2.224898×10^{-1}	-1.546151
a_5	-5.77054×10^{-4}	5.384366×10^{-5}	9.63994×10^{-5}
a_6	3.386979×10^{-7}	-4.904842×10^{-9}	-3.012151×10^{-9}
a_7	$-8.235686 \times 10^{-11}$	1.416132×10^{-13}	3.73735×10^{-14}

Table A.3. NASA-9 polynomial coefficients for C.

Coefficient	200–1000 K	1000–6000 K	6000–20000 K
a_1	4.496221×10^{5}	-8.924117×10^{7}	3.068442×10^{11}
a_2	-6.67958×10^{2}	1.190353×10^{5}	-1.997862×10^{8}
a_3	1.733875×10^{3}	1.831739×10^{3}	5.356055×10^{4}
a_4	-8.870894×10^{-3}	-2.32118×10^{-1}	-6.725457
a_5	1.370758×10^{-5}	1.205973×10^{-4}	4.603219×10^{-4}
a_6	-1.111862×10^{-8}	-2.009491×10^{-8}	-1.543784×10^{-8}
a_7	3.67898×10^{-12}	1.13681×10^{-12}	2.007118×10^{-13}

Table A.4. NASA-9 polynomial coefficients for O_2.

Coefficient	200–1000 K	1000–6000 K	6000–20000 K
a_1	-8.900882×10^{6}	-2.69695×10^{8}	1.292766×10^{11}
a_2	1.25943×10^{5}	6.092737×10^{5}	-7.447206×10^{7}
a_3	2.907605×10^{2}	4.728337×10^{3}	1.738401×10^{4}
a_4	1.115711	3.294337×10^{-1}	-1.603184
a_5	-1.776324×10^{-4}	-5.68541×10^{-5}	7.837713×10^{-5}
a_6	-5.257471×10^{-7}	5.336324×10^{-9}	-1.928359×10^{-9}
a_7	2.699811×10^{-10}	$-2.128966 \times 10^{-13}$	1.891139×10^{-14}

Table A.5. NASA-9 polynomial coefficients for CO.

Coefficient	200–1000 K	1000–6000 K	6000–20000 K
a_1	4.420005×10^{6}	1.371144×10^{8}	2.632527×10^{11}
a_2	-8.674362×10^{4}	-5.772574×10^{5}	-2.226373×10^{8}
a_3	1.699239×10^{3}	1.756288×10^{3}	7.407437×10^{4}
a_4	-2.426991	-1.681362×10^{-1}	-1.174383×10^{1}
a_5	4.324597×10^{-3}	4.152183×10^{-5}	9.788934×10^{-4}
a_6	-3.22881×10^{-6}	-5.306476×10^{-9}	-3.913499×10^{-8}
a_7	8.987985×10^{-10}	2.855838×10^{-13}	5.933543×10^{-13}